Wave-driven vortex dynamics in the surf zone

by

Andrea K. Barreiro

A dissertation submitted in partial fulfillment

of the requirements for the degree of

Doctor of Philosophy

Department of Mathematics

New York University

September 2006

Oliver Bühler—Advisor

Acknowledgements

I would like to thank my advisor, Oliver Bühler, for all of his time, patience, and good advice. I have had many useful discussions and taken great classes from many other Courant faculty, including K. Shafer Smith, Andrew J. Majda, Eric Vanden-Eijnden, Lai-Sang Young, Percy Deift, David Cai, Esteban Tabak, David Holland, and Olivier Pauluis.

I would like to thank all of my friends from RPI, Courant and elsewhere, who have given me so much love and support the last five years. Also more than a few hangovers, which might not have been so useful, but I can't say I regret them!

Finally I would like to thank my family and of course Robert Meyers, without whom you would not be reading this ground-breaking, brilliantly reasoned work that you are about to enjoy today.

Abstract

A longstanding problem in coastal oceanography is the prediction of the longshore currents that are forced by breaking waves in the surf zone. Traditional models based on a 1D momentum balance for the surf zone predict that current should be strongest in regions of the strongest wave breaking. However, current on a beach with a sandbar is sometimes observed to have a maximum in the "trough" of the bar, far from the region of maximum wave breaking.

In this thesis, we propose a mechanism for the development of this current based on vortex dynamics and show, based on idealized studies, that it can explain the broad features of the observed current. These studies are pursued using a new numerical model which exploits wave-mean interaction results in order to model the effect of breaking deep water waves, without resolving the waves themselves.

We focus on the role of wave group variation rather than bathymetric irregularities or shear waves, which we argue have been explored and found to be not enough to produce the expected behavior. Our first experiment examines beaches forced by isolated packets of obliquely incident waves. We find that current dislocation occurs on a barred beach (to the trough low) but not on a planar beach, and no dislocation occurs in the absence of wave group variations.

Our second experiment examines beaches forced by sinusoidally varying wave groups of the approximate spatial scale suggested by the observed wind speeds during the DELILAH experiment. We again find that current maxima develop in the trough region and that a relatively simple parameter, given the restricted set of forcings, will predict whether or not this occurs. This is a first step towards determining when realistically varying wave group forcing will produce current dislocation.

We also consider the existence of turbulence in shallow water with topography. We find that the physical scales governing the beach do not permit the development of vigorous two-dimensional turbulence, and specifically the generation of vortices larger than the spatial scale of circulation forcing.

Contents

List of Figures

List of Tables

Chapter 1

Introduction

For all of its history humankind has relied on the oceans for sustenance and travel. Today Earth's coastal regions are heavily populated and heavily touristed, so their study is not only of scientific interest but profound economic and social interest as well. The coastal ocean is a fantastically complex system: it contains the water, which is a fluid of varying density due to salinity, temperature, and the presence of other minerals and biological organisms; the bedrock and sediment, which can be transported in response to fluid motions; and the air above, whose currents are a primary forcing mechanism for ocean surface waves.

In this thesis I will focus on the generation of the current structure of coastal regions, specifically the generation of alongshore (parallel to the shoreline) currents. Such currents are primarily forced by the breaking of oblique surface waves and are affected by the local water depth, changes in bathymetry,

and wind forcing. The ability to accurately predict alongshore currents is necessary to prevent shoreline erosion [40] and to plan military water landings [47].

A quantitative theory of the generation of alongshore currents by obliquely incident sea waves was given by Longuet-Higgins [28, 29]. Several modelling assumptions were made in this work that have been adapted consistently by subsequent researchers. The instantaneous current is assumed to be horizontal or vertically-averaged. The forcing due to surface waves incoming from the open sea is modelled using the radiation stress theory developed earlier by Longuet-Higgins and Stewart [30, 31, 32, 33, 34], wherein surface gravity waves are found to impart a vertically-averaged momentum flux to the flow. Breaking and other dissipative processes cause convergence of this momentum flux, and therefore a forcing on the mean flow. Bottom friction is modelled by a quadratic function of the free stream velocity (as in a turbulent boundary layer[22]). However, because the mean velocity is taken to be small with respect to the wave velocity, this is approximated by a linear function of the mean velocity (where the constant coefficient is the mean orbital speed of the wave, or some spatial average thereof). Wind forcing is neglected, as in the surf zone it is generally thought to be much less important than wave forcing (reference here).

Finally, the bathymetry of the beach, wave forcing, and the mean current are assumed to be steady and one-dimensional: they do not vary in the alongshore direction. The result is a one-dimensional momentum balance which can

be solved for the mean alongshore current.

The general prediction of Longuet-Higgins is that alongshore current should develop in areas of wave breaking. The qualitative features of this current depend on the bathymetry of the beach, as well as the model for wave-breaking (itself a complicated and incompletely-understood process). On a planar beach, the current will have its maximum at the offshore onset of wave breaking, and will decrease in magnitude closer to the shoreline. On a barred beach, generally waves break as they slow down and increase in height over the bar, but then stop breaking as the water depth increases into the trough, and break again as they approach the shoreline. Therefore there should be a current on top of the bar and another closer to the shoreline.

Most subsequent developments have been modifications to this basic model. Various models for wave distribution and wave-breaking have been proposed [5, 54]. Reynold's stresses resulting from presumed turbulent motions are often included, parameterized as a turbulent eddy viscosity [28], while others argue that the vertical shear contributes to horizontal mixing and should be taken into account [53]. Many researchers also modify the wave dissipation model by adding a "surface roller" to the momentum balance[52]. A roller is the aerated body of water, produced by the overturning wave, which travels on top of the shoreward-traveling wave. The shear stress between the roller and the underlying wave dissipates energy and erodes the roller. According to these theoreticians, momentum from the wave is first transferred to the roller, and then to the mean flow as the roller subsides. The use of turbulent mixing

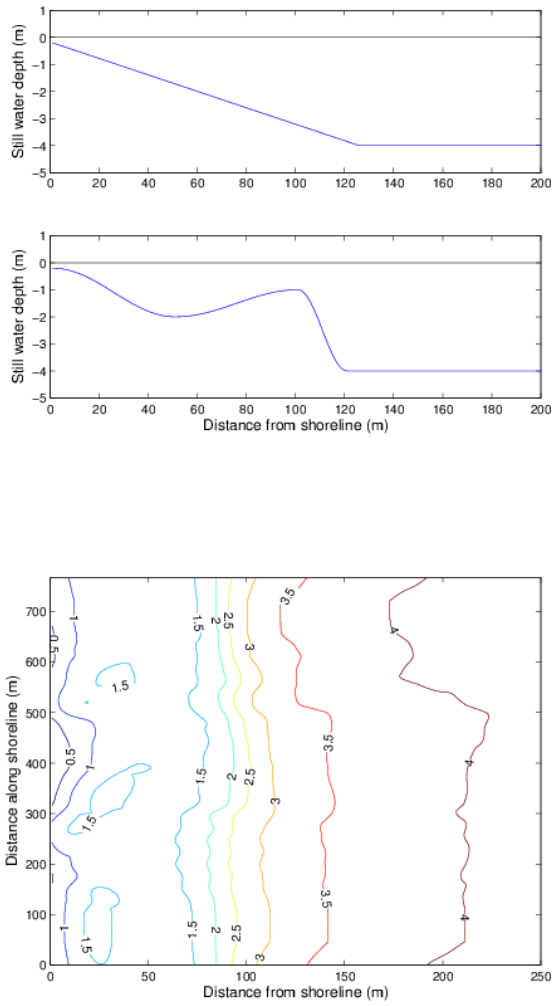

Figure 1.1: Planar vs. barred topography: profiles used in Chapter 5 (top); reconstructed topography from the DELILAH experiment (the data has been artificially extended near the domain boundaries to enforce periodicity)

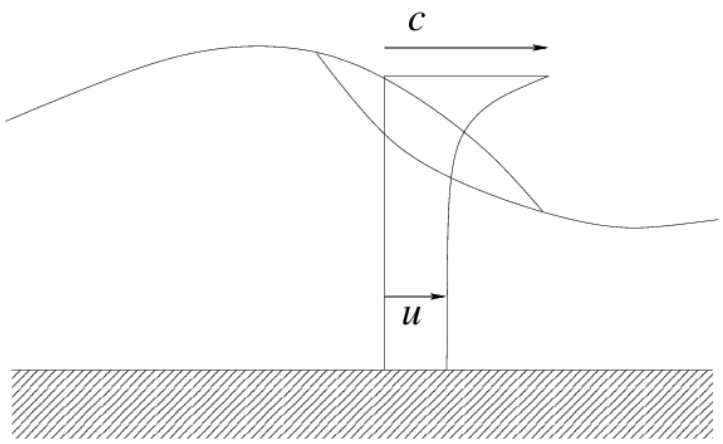

Figure 1.2: Schematic of surface roller, adapted from [52]. The roller travels at speed c meters per second, the phase speed of the travelling wave.

tends to smooth out predicted currents, whereas the use of surface rollers tend to move the location of the bar current somewhat seaward of the bar [41].

The one-dimensional momentum balance has been used with varying degrees of success to predict currents in experimental and laboratory settings. Field experiments have been performed at Santa Barbara in 1980[1], Duck NC

[1]Experiments were conducted as part of the Nearshore Sediment Transport Study (NSTS), Leadbetter Beach, CA, January 30-February 23 1980

in 1990[2], 1994[3] and 1997[4], and Edmonds, the Netherlands in 1995. The first beach is generally planar, the others generally barred (bathymetry naturally shifts over the course of the experiment). A one-dimensional model essentially like that of Longuet-Higgins is used with some success to match the data collected in Santa Barbara[55]. Predicted currents are broad and have a single maximum that is reasonably near (typically shorewards of) the experimental current maximum on a cross-shore transect.

On the barred beaches, however, the record is mixed. A laboratory experiment that explicitly enforced alongshore homogeneity[41] in the mean current and wavetrain on barred beaches found that two maxima developed, one over the bar and another near the shore, and that one-dimensional models that include surface rollers and an eddy viscosity could accurately reproduce the observed bar current. In experimental settings, however, the location of the alongshore current maximum varies significantly, from the crest of the bar to the trough. The most striking discrepancies occur in the DELILAH [13] experiment, where the alongshore current has a single maximum close to the trough of the beach for most days when there is a distinct alongshore bar in place [12] (before this period there are rhythmic, cusp-like ripples in the bathymetry; unfortunately significant current data is missing or has been discarded as unreliable after October 15, so it is not possible to extend this supposition any

[2]Duck Experiment on Low-frequency and Incident-Band Longshore and Across-shore Hydrodynamics (DELILAH), U.S. Army Corps of Engineers, Duck, NC, October 1-21 1990

[3]Duck94, U.S. Army Corps of Engineers, Duck, NC, August 8-24 and October 1-24, 1994

[4]SandyDuck, U.S. Army Corps of Engineers, Duck, NC, September 22-October 31, 1997

further).

So what went wrong? Assuming that all important physical forcing terms have been included in the momentum balance, either some forcing term is inadequately modelled or the assumption of alongshore inhomogeneity is not reasonable (or both). Feddersen et al. [15] examine the integrated momentum balance across a single cross-shore transect during Duck94 and conclude that it is "very unlikely" that there are other significant sources of momentum present. Ruessink et al. [48] examine alongshore velocities on a cross-shore measurement transect at Edmonds and Duck94 and compare with a model that uses rollers as part of its forcing parametrization. The inclusion of rollers in a one-dimensional momentum balance gives a better fit than without rollers. The authors restrict their study to time when the bathymetry is alongshore uniform, as measured by the following nondimensional metric

$$\chi^2 = \frac{1}{L_x L_y} \int_0^{L_x} \int_0^{L_y} \left(\frac{d(x,y) - \overline{d}(x)}{\overline{d}(x)} \right)^2 dy\, dx$$

This study, in conjunction with the experimental results of Reniers and Battjes[41], strongly suggests that, when uniform conditions are imposed or controlled for, our current understanding of the one-dimensional momentum balance is sufficient to describe the current.

Ruessink et al. [48] found that for $\chi^2 > 0.02$, the one-dimensional current model is not trustworthy, suggesting that bathymetric nonuniformities may play a role in "breaking"

Later Feddersen and Guza [14] examined alongshore inhomogeneity in the alongshore currents (now using data from several alongshore transects) in the 1997 SandyDuck experiments and found, contrary to previous results, that χ^2 does not correlate well with alongshore nonuniformities in the current.

Putrevu et al. [39] focus on the role that nonuniform bathymetry can play in current location on a planar beach with a sinusoidal alongshore variation. Using detailed scaling arguments, they argue that the largest terms in the alongshore momentum balance are the cross-shore gradient of the radiation stress and the alongshore gradient of the mean water height and compute profiles of the current velocity that indicate a shoreward shift. Reniers et al. [43] use the same procedure to examine a barred beach and also find that including bathymetric nonuniformities causes a shoreward shift. However, the current maximum is not shifted enough to match the data: it is shifted to about 70 m from shoreline, whereas the maximum current is measured at 50 m (a meter located at 70 m shows a current 20 percent smaller). In conclusion these theoretical models do not adequately explain the DELILAH observations, and later experiments do not show the result that bathymetric variations correlate to current variations, as is the case in these theoretical models.

Even with uniform bathymetry and wave forcing, non-uniformities can arise through the the propagation of so-called "shear waves", long propagating structures which appear to be related to a shear instability of a steady alongshore uniform current [7, 2, 49]. In fact, the spontaneous generation of wave-like current disturbances is probably the rule rather than the exception.

Slinn et al.[49] hypothesized that such instabilities could cause the cross-shore transport of alongshore momentum into the trough. They examine instabilities that arise in a realistic physical regime on an idealized barred beach. While the momentum appears to be "diffused" into the trough region, the current maxima are not shifted in this study, as required to replicate the DELILAH results.

Another source of inhomogeneity is in the wave forcing. Longuet-Higgins, and most others, consider a wavetrain that is alongshore uniform and monochromatic. Most wavetrains however are not monochromatic and a directional spread is known to cause "surf-beats" [32]. The interactions of monochromatic waves with edge waves can also create alongshore variations in the wave height, and have been shown to form circulation cells in the laboratory [8]. The effect of inhomogeneity was considered by Bowen [6] and Komar [25] in the form of an alongshore variation of breaker height. Bowen and Komar recognized that alongshore differences in wave breaking will produce variations in wave set-up, or the mean water level. This is turn forces a current away from the locations of higher mean water level (high breaker) towards locations of low mean water level. This effect was revisted by Reniers et al.[44] in the context of using short-wave frequency spectra to predict subharmonic motions (the "surf-beat" generated by groupy short waves). The authors found that the subharmonic wave energy was well modelled by the linear relationship between wave groups during the DELILAH experiment. In a later paper Reniers et al.[42] examine the evolution of bathymetry under the forcing of short wave

groups. The wave forcing is produced by generating random time series that have a realistic frequency distribution. Examination of an example time series is instructive (see [42], Figure 4); the wave energy at a given point varies up to a fraction of less than 5% of its peak value over time, with a quasi-periodic structure of about 40 seconds. If we translate this structure to oblique waves (in [42] only waves of 0° average direction are considered), we see that this variation in wave energy is instantaneously present along an alongshore transect (including the bar crest).

We will argue that large scale variations in wave height, such as those caused by realistic groupiness of short waves, can explain current dislocation on a barred beach through vortex dynamics. The breaking of non-uniform waves forces vortex dipoles in the mean flow, whose evolution inherently promotes dislocation of current on barred beaches, but not on planar beaches (where this effect has not been pronounced in experimentation).

We will use an unsteady, two-dimensional, potential-vorticity based numerical model to evolve nearshore currents. With this method we avoid the explicit computation of wave set-up which is crucial to Putrevu's method [39, 43]. We will explicitly resolve the radiation stress and therefore will not rely on the scaling assumptions made in those papers. In Chapter 2, we justify the equations used in our numerical model, which include an open boundary condition for the seaward end. In Chapter 3, we explain more fully past models for current prediction and our own. In Chapter 4, we present our numerical model. Chapter 5 presents an idealized experiment that produces the expected cur-

rent structure. In Chapter 6, we pursue an experiment motivated by references [44, 42] wherein we examine the currents produced by sinusoidal wave-groups breaking on a barred beach.

Finally we address, in Chapter 7, the question of to what extent the large-scale surf zone currents are turbulent. This is relevant to whether or not vorticity structures may be formed by an upscale energy cascade, as suggested by Peregrine[37].

Chapter 2

The Shallow-Water Equations

2.1 Basic properties of shallow-water equations in a finite domain

We begin with the free-surface shallow-water equations with variable bottom topography[1]. The dynamic variables are the layer depth $h(x, y, t)$ and the two-dimensional horizontal velocity $\boldsymbol{u}(x, y, t) = (u, v)$. The governing equations are

[1]The words "topography" and "bathymetry" are used intechangeably in this document to indicate variations in the elevation of the ocean floor. "Bathymetry" is used in the coastal oceanography literature, whereas "topography" is common in the applied mathematics literature (perhaps because of a closer connection with atmospheric scientists).

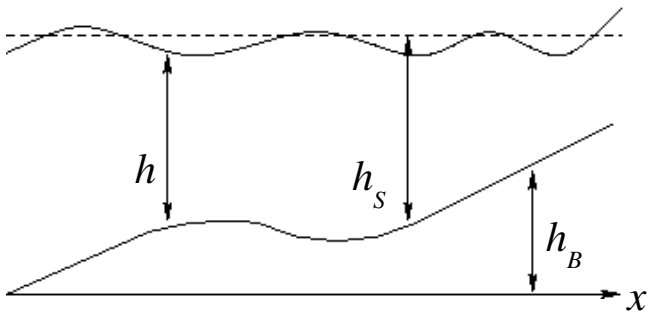

Figure 2.1: Schematic cross-section of variable depth topography, demonstrating the definitions of the height variables h,h_S, and h_B

$$\begin{aligned} \frac{\partial h}{\partial t} + \nabla \cdot (h\boldsymbol{u}) &= 0 \\ \frac{D\boldsymbol{u}}{Dt} + g\nabla(h + h_B) &= \boldsymbol{F} - \frac{c_f}{h}|\boldsymbol{u}|\boldsymbol{u} \end{aligned}$$

where h_B is the bottom elevation, as shown in 2.1 here), $\boldsymbol{F}$ is an unspecified body force, and c_f is a coefficient for quadratic bottom friction. h may be written as the sum of the still water depth h_S and a deflection, so that $h = h_S + h'$ and $h_S + h_B = h_{S_0}$. A dynamic equation for the potential vorticity can be given

$$
\begin{aligned}
q &\equiv \frac{\nabla \times \boldsymbol{u}}{h} \\
\frac{Dq}{Dt} &= \frac{\nabla \times \boldsymbol{F}}{h} - \frac{c_f}{h} \nabla \times \left(\frac{|\boldsymbol{u}|\boldsymbol{u}}{h} \right)
\end{aligned}
$$

Generally we will be concerned with these equations in the case of low Froude number (ratio of typical flow speed to gravity wave speed). We non-dimensionalize the equations by standard velocity, length and time scales (U, L, T respectively), and assume depth deflections above the still water depth to be on the scale of U^2. Finally, we assume that $U \approx \epsilon\sqrt{gh_S}$[2]. Collecting terms at order ϵ, we find

$$
\begin{aligned}
\nabla \cdot (h_S \boldsymbol{u}) &= 0 && (2.1) \\
\frac{D\boldsymbol{u}}{Dt} + g\nabla(h') &= \boldsymbol{F} - \frac{c_f}{h_S}|\boldsymbol{u}|\boldsymbol{u} && (2.2)
\end{aligned}
$$

Defining $p = g\rho h'$, we will henceforth think of this system of equations as describing a layer of fluid with a "rigid lid". p is the pressure at the still water depth due to the weight of the fluid above it.

The rigid-lid shallow-water equations may now be written as

$$
\begin{aligned}
\nabla \cdot (h_S \boldsymbol{u}) &= 0 && (2.3) \\
\frac{D\boldsymbol{u}}{Dt} + \frac{1}{\rho}\nabla p &= \boldsymbol{F} - \frac{c_f}{h_S}|\boldsymbol{u}|\boldsymbol{u} && (2.4)
\end{aligned}
$$

[2]For our purposes, $U < 1\ m$ whereas $\sqrt{gh} \approx 6m/s$

where h_S is the still water depth, p is the pressure at the rigid lid, and ρ is the fluid density (which we will always take to be constant).

We consider the equations for u, v in the domain $0 \leq x \leq D$, $0 \leq y \leq L$, periodic in the y direction. The boundary conditions in the x-direction are no-normal flow; that is $u(0, y, t) = u(D, y, t) = 0$. Because $h_S \boldsymbol{u}$ is a non-divergent vector field, a stream function ψ can be defined, unique up to a constant, for which

$$\begin{aligned} h_S u &= -\frac{\partial \psi}{\partial y} \\ h_S v &= \frac{\partial \psi}{\partial x} \end{aligned}$$

Then ψ and q satisfy the following equation:

$$\nabla \cdot \left(\frac{\nabla \psi}{h_S} \right) = h_S q \tag{2.5}$$

$$\frac{Dq}{Dt} = \frac{\nabla \times \boldsymbol{F}}{h} - \frac{c_f}{h} \nabla \times \left(\frac{|\boldsymbol{u}| \boldsymbol{u}}{h} \right) \tag{2.6}$$

The second equation is the dynamic equation for vorticity, which has been previously stated.

With the appropriate boundary conditions, and assuming $h_S > 0$ throughout the domain, ψ is uniquely determined by q. The continuity equation implies that ψ is periodic. By the no-normal flow boundary condition, we must have $\psi(0, y) = A_0$ and $\psi(D, y) = A_D$, where $A_0(t)$, $A_D(t)$ are constant in y but may evolve in time (without loss of generality we take $A_0 = 0$). It is

easy to verify the following fact:

Proposition 1. *The solution ψ to (2.5), given $q(x,y,t)$, is unique for either of the following sets of boundary conditions:*

1. $\psi(0,y,t) = 0$, $\psi(D,y,t) = A_D$
2. $\psi(0,y,t) = 0$, $\int_0^L \frac{1}{h_S}\frac{\partial\psi}{\partial x}\,dy = C_D$, $\psi(D,y,t)$ *constant in y but not known.*

Proof. Because (2.5) is linear, it is sufficient to show that the homogeneous equation with either $A_D = 0$ or $C_D = 0$ can have only the zero solution. That is, let ψ_1, ψ_2 be two solutions to (2.5), with $\psi_1(D,y,t) = \psi_2(D,y,t) = A_D$. Then we wish to show that $\psi_1 - \psi_2 = 0$.

Consider (2.5) where $q \equiv 0$. Multiply by ψ and integrate over the domain. We have

$$\begin{aligned} 0 &= \int_0^D \int_0^L \psi \nabla \cdot \left(\frac{\nabla\psi}{h_S}\right)\,dy\,dx \\ &= -\int_0^D \int_0^L \frac{1}{h_S}|\nabla\psi|^2\,dy\,dx + \left[\int_0^L \frac{1}{h_S}\psi\frac{\partial\psi}{\partial x}\,dy\right]_0^D + \left[\int_0^D \frac{1}{h_S}\psi\frac{\partial\psi}{\partial y}\,dx\right]_0^L \end{aligned}$$

The third term is zero by periodicity. Suppose that $A_D = 0$; then the second term is zero as well. If $C_D = 0$, but $\psi(D,y,t)$ is constant in y, then the second term may be written

$$\begin{aligned} \left[\int_0^L \frac{1}{h_S}\psi\frac{\partial\psi}{\partial x}\,dy\right]_0^D &= \left[\psi\int_0^L \frac{1}{h_S}\frac{\partial\psi}{\partial x}\,dy\right]_0^D \\ &= \psi(D,y,t)\int_0^L \frac{1}{h_S}\frac{\partial\psi}{\partial x}\,dy \end{aligned}$$

The integral is precisely C_D, so this term is zero as well. □

Proposition 2. *A_D and C_D satisfy the following time-tendency equations.*

$$\frac{dA}{dt} = \frac{1}{L}\int_0^D \int_0^L h_S \boldsymbol{F}_y - c_f v|\boldsymbol{u}| + p\frac{\partial h_S}{\partial y}\, dy\, dx \tag{2.7}$$

$$\frac{dC}{dt} = \frac{1}{L}\int_0^L \boldsymbol{F}_y(D,y) - c_f \frac{v(D,y)|\boldsymbol{u}(D,y)|}{h_S}\, dy \tag{2.8}$$

Proof. For the first statement, we observe, using the fact that $\psi(D,y,t)$ is constant in y, that

$$\begin{aligned}\psi(D,y,t) &= \int_0^D \frac{\partial \psi}{\partial x}\, dx \\ &= \frac{1}{L}\int_0^L \int_0^D \frac{\partial \psi}{\partial x}\, dx\, dy \\ &= \frac{1}{L}\int_0^L \int_0^D h_S v\, dx\, dy\end{aligned}$$

Then

$$\begin{aligned}\frac{\partial \psi}{\partial t}(D,y,t) &= \frac{1}{L}\int_0^L \int_0^D h_S \frac{\partial v}{\partial t}\, dx\, dy \\ &= \frac{1}{L}\int_0^L \int_0^D h_S \left(-u\frac{\partial v}{\partial x} - v\frac{\partial v}{\partial y} + \boldsymbol{F}_y - c_f\frac{v|\boldsymbol{u}|}{h_S} - \frac{\partial p}{\partial y}\right) dx\, dy\end{aligned}$$

The final term in (2.7) can be obtained by integration by parts, using the

periodicity of p:

$$\frac{1}{L}\int_0^D\int_0^L h_S\frac{\partial p}{\partial y}\,dy\,dx \;=\; \frac{1}{L}\int_0^D\int_0^L -p\frac{\partial h_S}{\partial y}\,dy\,dx$$

The Jacobian can be shown to vanish by the following:

$$\begin{aligned}\frac{1}{L}\int_0^D\int_0^L\left[-h_S u\frac{\partial v}{\partial x}-h_S v\frac{\partial u}{\partial y}\right]\,dy\,dx &= \frac{1}{L}\int_0^D\int_0^L\left[\frac{\partial\psi}{\partial y}\frac{\partial v}{\partial x}-\frac{\partial\psi}{\partial x}\frac{\partial u}{\partial y}\right]\,dy\,dx\\ &= \frac{1}{L}\left[\int_0^D\psi\frac{\partial v}{\partial x}\,dx\right]_0^L-\frac{1}{L}\int_0^D\int_0^L\psi\frac{\partial^2 v}{\partial y\partial x}\,dy\,dx\\ &\quad -\frac{1}{L}\left[\int_0^L\psi\frac{\partial v}{\partial y}\,dy\right]_0^D+\frac{1}{L}\int_0^D\int_0^L\psi\frac{\partial^2 v}{\partial x\partial y}\,dy\,dx\\ &= 0\end{aligned}$$

The first boundary term vanishes by periodicity, the second by using constancy of ψ at the x boundaries and periodicity of v. The double integrals cancel.

The second statement follows from the identity that $v=\frac{1}{h_S}\frac{\partial\psi}{\partial x}$. Then

$$\begin{aligned}C_D &= \frac{1}{L}\int_0^L\frac{1}{h_S}\frac{\partial\psi}{\partial x}(D,y,t)\,dy\\ &= \frac{1}{L}\int_0^L v(D,y,t)\,dy\\ \frac{\partial C_D}{\partial t} &= \frac{1}{L}\int_0^L\frac{\partial v}{\partial t}(D,y,t)\,dy\\ &= \frac{1}{L}\int_0^L\left[-u\frac{\partial v}{\partial x}-v\frac{\partial v}{\partial y}-\frac{\partial p}{\partial y}-c_f\frac{v|\boldsymbol{u}|}{h_S}+\boldsymbol{F}_y\right]\,dy\end{aligned}$$

The pressure term vanishes by periodicity. The advection terms, as in the case

with A_D, vanish by integration by parts.

□

The previous proposition motivates the use of C_D as a constraint. While computing the time-tendency of A_D requires computation of the pressure unless h is independent of y, C_D never requires the pressure.

Proposition 3. *The equations (2.3,2.4) are equivalent to (2.5,2.6)*

Proof. That a solution to (2.3,2.4) also solves (2.5,2.6) has already been established by differentiation and uniqueness of the stream function inversion equation.

Conversely, if ψ and q satisfy (2.5,2.6), then the velocity field defined by $h_S\boldsymbol{u} = \nabla^\perp\psi$ satisfies (2.3,2.4) for the gradient of some potential ∇p. By taking the divergence of the velocity equations we recover an elliptic equation for p

$$\nabla \cdot (-h_S \nabla p) \;=\; \nabla \cdot (J(\psi, \boldsymbol{u})) - \nabla \cdot (h_S \boldsymbol{F}) + c_f \nabla \cdot (\boldsymbol{u}|\boldsymbol{u}|)$$

With the boundary conditions, $\frac{\partial p}{\partial x}(0, y) = \frac{\partial p}{\partial x}(D, y) = 0$, p is determined uniquely up to a constant. □

Proposition 4. *The shallow-water equations with a rigid lid conserve the following quantities in the absence of forcing and dissipation ($\boldsymbol{F} = 0$, $c_f = 0$)*

1. *Kinetic energy:* $\frac{1}{2}\int_0^D \int_0^L h_S(u^2 + v^2)\, dy\, dx$
2. *Enstrophy:* $\frac{1}{2}\int_0^D \int_0^L h_S q^2\, dy\, dx$

3. *Circulation:* $\int_0^D \int_0^L h_S q \, dy \, dx$

4. *In the event that* $h_S(x, y) \equiv h_S(x)$*, then solutions also conserve alongshore momentum* $\int_0^D \int_0^L h_S v \, dx \, dy$

2.2 Extension to infinite domain and "exact" boundary conditions

We wish to extend the previous state of knowledge about the finite domain into the case of the shallow-water equations with a rigid lid in the domain $0 \leq x < \infty$, $0 \leq y \leq L$. The boundary conditions at infinity are that $\boldsymbol{u} \to 0$. In this case, we have to make some assumptions about h_S. Let us suppose that $h_S = 1$ for $x \geq D$.

We introduce the following boundary condition, the Dirichlet-to-Neumann (DtN) boundary condition [23, 18]. We wish to show that the problem with the DtN boundary condition at the seaward end of a finite domain (the "interior domain") has the same solution as the problem on the infinite domain, where $q \equiv 0$ in the "exterior domain". Thus, the infinite domain problem ($0 \leq x < \infty$) can be exactly computed on a finite domain ($0 \leq x \leq D$).

The DtN boundary condition for any partial differential equation problem is meant to replace a Dirichlet, Neumann, or mixed condition on the boundary. It gives a constraint on the relationship between the Dirichlet data and the normal derivative at the boundary. Typically, it enforces the relationship that

is present in a "decaying" mode of a solution. Therefore it is well-suited to pick out a restriction of a solution that is bounded in an infinite domain.

By way of illustration, we examine the following one-dimensional problem. Consider the equation

$$\begin{aligned} \frac{\partial^2 \psi}{\partial x^2} &= q(x), & 0 < x < D \\ \frac{\partial^2 \psi}{\partial x^2} &= 0, & x \geq D \end{aligned}$$

Then $\psi(x)$, for $x > D$, must be a linear combination of the two linearly independent solutions to the differential equation: $\psi(x) = Ae^x + Be^{-x}$. If the solution is to be bounded, clearly there must be no contribution from e^x. Imposing the boundary condition

$$\frac{\partial \psi}{\partial x} = -\psi$$

at $x = D$ ensures that the solution beyond that point can only contain the decaying mode.

For the current case we define the DtN map to be the following:

$$\begin{aligned} \frac{\partial \psi}{\partial x}(D, y) &= \frac{1}{L} \sum_0^\infty \left[-\frac{4\pi k}{L} \left[\int_0^L \psi(D, t) cos \left(\frac{2\pi k}{L}(y - t) \right) \, dt \right] \right] \\ &\equiv M\psi(D, y) \end{aligned}$$

This expression will be justified at the end of this section, but first we establish

properties of the solution.

Proposition 5. *Let ψ solve (2.5) for q continuous, in the domain $0 \le x \le D$, $0 \le y \le L$. For boundary conditions, we take $\psi(0,y) = 0$, $\frac{\partial \psi}{\partial x}(D,y) = M\psi(D,y)$, and $\psi(x,y) = \psi(x,y+L)$. Then ψ is unique.*

Proof. To show uniqueness, we show that the only solution to

$$\begin{aligned} \nabla \cdot \left(\frac{\nabla \psi}{h_S} \right) &= 0 \qquad 0 < x < D \\ \psi(x,0) &= \psi(x,L) \\ \psi(0,y) &= 0 \\ \frac{\partial \psi}{\partial x}(D,y) &= M\psi(D,y) \end{aligned}$$

is $\psi(x,y) = 0$.

$$\begin{aligned} \int_0^D \int_0^L \psi \nabla \cdot \left(\frac{\nabla \psi}{h_S} \right) \, dy \, dx &= -\int_0^D \int_0^L \frac{1}{h_S} |\nabla \psi|^2 \, dy \, dx + \left[\int_0^L \frac{1}{h_S} \psi \frac{\partial \psi}{\partial x} \, dy \right]_0^D \\ &\quad + \left[\int_0^D \frac{1}{h_S} \psi \frac{\partial \psi}{\partial y} \, dx \right]_0^L \qquad (2.9) \\ &= 0 \end{aligned}$$

The third term in the right hand side of (2.9) vanishes by periodicity. Using

the boundary conditions, we can write

$$\begin{aligned}\left[\int_0^L \frac{1}{h_S}\psi\frac{\partial\psi}{\partial x}\,dy\right]_0^D &= \int_0^L \frac{1}{h_S}\psi(D,y)\frac{\partial\psi}{\partial x}(D,y)\,dy \\ &= \int_0^L \frac{1}{h_S}\left[\sum_{k\geq 0}\hat{\psi}_{c,k}\cos\left(\frac{2\pi k}{L}y\right)+\sum_{k>0}\hat{\psi}_{s,k}\sin\left(\frac{2\pi k}{L}y\right)\right]\times \\ &\quad \left[\sum_{k\geq 0}\left(-\frac{4\pi k}{L}\right)\cos\left(\frac{2\pi k}{L}y\right)\hat{\psi}_{c,k}\right]\,dy\end{aligned}$$

where we define

$$\begin{aligned}\hat{\psi}_{c,k} &\equiv \frac{1}{L}\int_0^L \psi(D,t)\cos\left(-\frac{2\pi k}{L}t\right)\,dt \qquad k\geq 0 \\ \hat{\psi}_{s,k} &\equiv \frac{1}{L}\int_0^L \psi(D,t)\sin\left(-\frac{2\pi k}{L}t\right)\,dt \qquad k>0\end{aligned}$$

These Fourier coefficients have been normalized so that

$$\psi(D,y)=\sum_{k\geq 0}\hat{\psi}_{c,k}\cos\left(\frac{2\pi k}{L}y\right)+\sum_{k>0}\hat{\psi}_{s,k}\sin\left(\frac{2\pi k}{L}y\right)$$

Using the orthogonality of the trigonometric functions we find

$$\int_0^D\int_0^L \frac{1}{h_S}|\nabla\psi|^2\,dy\,dx = \sum_{k\geq 0}\left(-\frac{4\pi k}{L}\right)\frac{L}{2}\hat{\psi}_{c,k}^2$$

which implies that $\psi(x,y)\equiv 0$.

□

Finally, we wish to justify (2.9). The key is to solve the elliptic problem on the exterior domain for general Dirichlet data, and to extract the DtN map from this solution. Then if we solve the problem in the interior domain with the DtN boundary condition, we can imagine constructing a continuation of this solution into the exterior. This continuation will "fit together" smoothly with the interior solution because of the way we have constrained the derivatives at the boundary.

The following calculation can and has been done for various geometries, such as the outside of a circle [23], sphere [18], or ellipse [18]. A methodology has also been given for geometries of very general shape [16][3]. Here we are interested in a periodic strip.

Assume that $h(x, y) = 1$ outside of the domain $x \in [0, D]$. Then the exterior Dirichlet problem, given boundary data at $x = D$, can be written as

$$\nabla^2 \psi(x, y) = 0 \tag{2.10}$$

$$\psi(D, y) = p(y) \tag{2.11}$$

We can write the solution to this equation [1] as

$$\psi(x, y) = \frac{x - D}{\pi} \int_{-\infty}^{\infty} \frac{p(t)}{(x - D)^2 + (y - t)^2} \, dt \tag{2.12}$$

[3] A general review of developments can be found in reference [56]

Because $p(y)$ is periodic, we can write

$$\begin{aligned}\psi(x,y) &= \frac{x-D}{\pi}\int_0^L p(t)\left[\sum_{n=-\infty}^{\infty}\frac{1}{(x-D)^2+(y-nL-t)^2}\right]\,dt \quad (2.13)\\ &= G_x * p(y) \quad (2.14)\end{aligned}$$

where

$$G_x(y) = \frac{x-D}{\pi}\sum_{n=-\infty}^{\infty}\frac{1}{(x-D)^2+(y-nL)^2}$$

Define the Fourier coefficients $\hat{u}_k = \frac{1}{\sqrt{L}}\int_0^L u(y)e^{-2\pi iky/L}dy$. Then

$$\begin{aligned}\hat{\psi}_k(x) &= \hat{G}_{xk}\hat{p}_k \quad (2.15)\\ \frac{\partial\hat{\psi}_k(x)}{\partial x} &= \frac{\partial\hat{G}_{xk}}{\partial x}\hat{p}_k \quad (2.16)\\ \frac{\partial\psi(x,y)}{\partial x} &= \frac{1}{\sqrt{L}}\sum_{k=-\infty}^{\infty}\left[\frac{\partial\hat{G}_{xk}}{\partial x}\hat{p}_k\right]e^{2\pi iky/L} \quad (2.17)\\ &= \frac{1}{\sqrt{L}}\sum_{k=-\infty}^{\infty}\left[\frac{\partial\hat{G}_{xk}}{\partial x}\left[\frac{1}{\sqrt{L}}\int_0^L\psi(D,t)e^{2\pi ik(y-t)/L}\,dt\right]\right]. \quad (2.18)\end{aligned}$$

In particular, for $x = D$

$$\frac{\partial\psi(D,y)}{\partial x} = \frac{1}{L}\sum_{k=-\infty}^{\infty}\left[\frac{\partial\hat{G}_{xk}(D)}{\partial x}\left[\int_0^L\psi(D,t)e^{2\pi ik(y-t)/L}\,dt\right]\right]. \quad (2.19)$$

We find by complex integration that $\hat{G}_{xk} = e^{-2\pi(x-D)|k|/L}$ for $k \neq 0$, and

$\hat{G}_{x0} = 1$. Therefore

$$\frac{\partial \hat{G}_{xk}}{\partial x} = -\frac{2\pi|k|}{L}\hat{G}_{xk} \tag{2.20}$$

$$\frac{\partial \hat{G}_{xk}}{\partial x}(D) = -\frac{2\pi|k|}{L} \tag{2.21}$$

This expression is valid for all k.

Using the reality condition we re-write

$$\frac{\partial \psi(D,y)}{\partial x} = \frac{1}{L}\sum_{k=0}^{\infty}\left[-\frac{4\pi k}{L}\left[\int_0^L \psi(D,t)\cos\left(\frac{2\pi k}{L}(y-t)\right)dt\right]\right] \tag{2.22}$$

We cannot "switch" the integral and sum, because the sum is not convergent. However, for any finite truncation, we can interchange and write the following:

$$\frac{\partial \psi(D,y)}{\partial x} = \frac{1}{L}\left[\int_0^L \psi(D,t)\sum_{k=0}^{K}\left[-\frac{4\pi k}{L}\cos\left(\frac{2\pi k}{L}(y-t)\right)\right]dt\right] \tag{2.23}$$

2.3 An analysis of the mean flow dynamics using wave-mean interactions

As we have noted, a common assumption in numerical models of shallow water with low Froude number flows ($U \ll \sqrt{gh_S}$, where U is a characteristic velocity

of the flow and h_S is the still depth of the fluid layer; i.e. $\sqrt{gh_S}$ is the speed of surface gravity waves) is to use the "rigid-lid" assumption. Here, I summarize an argument from reference [10] that in the presence of small-amplitude waves (whose amplitude can be measured by the small, non-dimensional number a), to $O(a^2)$, the mean velocity (in a sense that we shall define) evolves according to rigid-lid dynamics.

The governing equations that we are concerned with are

$$\frac{\partial h}{\partial t} + \nabla \cdot (h\boldsymbol{u}) = 0 \tag{2.24}$$

$$\frac{Du}{Dt} + g\nabla(h + h_B) = \boldsymbol{F} - \frac{c_f}{h}|\boldsymbol{u}|\boldsymbol{u} \tag{2.25}$$

We will assume that all flow fields ϕ can be split into a mean part $\overline{\phi}$ and disturbance part ϕ' such that $\phi = \overline{\phi}+\phi'$. The mean part is defined by time-averaging over one wavelength of the waves; that is $\overline{\phi(\boldsymbol{x},t)} = \frac{\omega}{2\pi}\int_t^{t+\frac{2\pi}{\omega}} \phi(\boldsymbol{x},s)ds$. We assume that all mean variables are slowly varying in the horizontal; that is, if the gradient of ϕ is $O(1)$, then the gradient of $\overline{\phi}$ is $O(\mu) \ll 1$.

We wish to consider the mean-flow response to slowly-varying small-amplitude gravity waves propagating on a state of rest. Formally, we introduce a non-dimensional wave amplitude a such the background (rest) state is $O(1)$, the wave field is $O(a)$, and the mean-flow response is $O(a^2)$. The $O(1)$ background state has zero velocity and a flat surface. The rest state is then $h(\boldsymbol{x},t) = h_S(\boldsymbol{x}) = h_{S_0} - h_B(\boldsymbol{x})$, where h_{S_0} is some reference depth and $h_B(\boldsymbol{x})$ is the height of the bottom, and $u(\boldsymbol{x},t) = 0$. To find the governing equations

for linear gravity waves, we set $\boldsymbol{u} = \boldsymbol{u}' + O(a^2)$, $h = h_S + h' + O(a^2)$ and find that the $O(a)$ terms of (2.24,2.25) are

$$\begin{aligned} \frac{\partial h'}{\partial t} + \nabla \cdot (h_S \boldsymbol{u}') &= 0 \\ \frac{\partial \boldsymbol{u}'}{\partial t} + g \nabla h' &= \boldsymbol{F}' \end{aligned}$$

For $\boldsymbol{F}' = 0$, these admit irrotational, nondispersive gravity waves

$$\begin{aligned} \boldsymbol{u}'(\boldsymbol{x}, t) &= a\sqrt{g h_S} \cos(\boldsymbol{k} \cdot \boldsymbol{x} - \omega t) \frac{\boldsymbol{k}}{\kappa} \\ h'(\boldsymbol{x}, t) &= a h_S \cos(\boldsymbol{k} \cdot \boldsymbol{x} - \omega t) \end{aligned} \tag{2.26}$$

where $\kappa = |\boldsymbol{k}|$ and $\omega = \sqrt{g h_S}\kappa$.

Let us also introduce the linear particle displacement[4]

$$\frac{\partial \boldsymbol{\xi}'}{\partial t}(\boldsymbol{x}, t) = \boldsymbol{u}'(\boldsymbol{x}, t)$$

This implies that

$$h' + \nabla \cdot (h_S \boldsymbol{\xi}') = 0$$

[4]This is not the same particle displacement defined in the Generalized Lagrangian Mean (GLM) theory; nothing that follows relies on GLM in any way, although the results produced do have a counterpart in GLM [3]

I can now define the Lagrangian mean quantity

$$\bar{\phi}^L(\boldsymbol{x},t) \equiv \overline{\phi(\boldsymbol{x}+\boldsymbol{\xi}'(\boldsymbol{x},t),t)}$$

and the Stokes drift of ϕ

$$\bar{\phi}^S \equiv \bar{\phi}^L - \overline{\phi}$$

Using Taylor expansions I can write $\bar{\phi}^S$ in terms of the linear particle displacement; e.g., $\bar{\boldsymbol{u}}^S$ is given, with an error of $O(a^3)$ as long as $\boldsymbol{u}$ is $O(a)$ or smaller, as

$$\begin{aligned}
\bar{\boldsymbol{u}}_i^S &= \overline{\xi_j' u_{i,j}'} \\
\bar{\boldsymbol{u}}^S &= \overline{(\boldsymbol{\xi}'\cdot\nabla)\boldsymbol{u}'} \\
&= \frac{1}{h_S}\overline{(h_S\boldsymbol{\xi}'\cdot\nabla)\boldsymbol{u}'} \\
&= -\frac{1}{h_S}\overline{\nabla\cdot(h_S\boldsymbol{\xi}')\boldsymbol{u}'} + O(\mu a^2) \\
&\approx \frac{1}{h_S}\overline{h'\boldsymbol{u}'}
\end{aligned}$$

The boundary term is neglected because it is a derivative of an averaged quantity, and therefore is small compared to its magnitude.

The wave energy per unit mass is defined to be

$$E = \frac{1}{2}\left(\overline{u'^2} + \overline{v'^2} + g\frac{\overline{h'^2}}{h_S}\right)$$

We will also introduce the psuedomomentum vector, which will be defined as

$$\begin{aligned}
\mathbf{p}_i &= -\overline{\xi'_{j,i}u'_j} \\
&\approx \overline{\xi'_j u'_{i,j}} + \overline{\xi'_j(u'_{j,i} - u'_{i,j})} \\
\mathbf{p} &\approx \bar{u}^S + \overline{\boldsymbol{\xi}' \times \hat{z}(\nabla \times \boldsymbol{u}')}
\end{aligned}$$

We will find that $\mathbf{p}$ is linked to the dissipative forcing of the mean flow.

Using the definition of $\boldsymbol{\xi}'$ and the equations satisfied by the linear gravity waves[34, 10], we find that the change in time of $\mathbf{p}$ is given by

$$\begin{aligned}
\frac{\partial \mathbf{p}_i}{\partial t} + \frac{1}{h_S}\frac{\partial}{\partial x_j}\left(h_S\overline{u'_i u'_j} + \delta_{ij}\frac{h_S}{2}\left[g\frac{\overline{h'^2}}{h_S} - \overline{|\boldsymbol{u}'|^2}\right]\right) + \frac{\overline{|\boldsymbol{u}'|^2}}{2h_S}\frac{\partial h_S}{\partial x_i} &= -\overline{\xi'_{j,i}F'_j} \\
&\equiv \mathscr{F}_i
\end{aligned}$$

2.3.1 Mean-flow response, early stage

We begin by averaging the continuity (2.24) and momentum (2.25) equations, using the fact that $\overline{\phi'} = 0$ for any ϕ. The continuity equation becomes

$$\frac{\partial \bar{h}}{\partial t} + \nabla \cdot (\overline{h}\overline{\boldsymbol{u}} + \overline{h'\boldsymbol{u}'}) = 0$$

I define the "depth set-up" $\overline{\Delta h} \equiv \overline{h} - h_S$.[5] Then

$$\frac{\partial \overline{\Delta h}}{\partial t} + \nabla \cdot (h_S \bar{\boldsymbol{u}}^L) = 0$$

Averaging the momentum equation (without the friction term, which is still negligible at $O(a^2)$) gives

$$\frac{\partial \overline{\boldsymbol{u}}}{\partial t} + (\boldsymbol{u} \cdot \nabla)\boldsymbol{u} + \overline{(\boldsymbol{u}' \cdot \nabla)\boldsymbol{u}'} + g\nabla(\overline{h} + h_B) = \overline{\boldsymbol{F}}$$

By neglecting terms at higher order than $O(a^2)$ and using $\overline{\Delta h}$, we find

$$\frac{\partial \overline{\boldsymbol{u}}}{\partial t} + \overline{(\boldsymbol{u}' \cdot \nabla)\boldsymbol{u}'} + g\nabla\overline{\Delta h} = \overline{\boldsymbol{F}}$$

We can manipulate the advection term in the previous equation, using again the linear gravity wave solution, to get

$$\frac{\partial \bar{\boldsymbol{u}}^L}{\partial t} + \frac{1}{h_S}\nabla \cdot \left(h_S \overline{\boldsymbol{u}'\boldsymbol{u}'} + \boldsymbol{\delta}\frac{g}{2}\overline{h'^2} \right) + g\nabla\overline{\Delta h} = \bar{\boldsymbol{F}}^L$$

or,

$$\begin{aligned} \frac{\partial \bar{\boldsymbol{u}}^L}{\partial t} + g\nabla\overline{\Delta h} &= -\frac{1}{h_S}\nabla \cdot \left(h_S \overline{\boldsymbol{u}'\boldsymbol{u}'} + \boldsymbol{\delta}\frac{g}{2}\overline{h'^2} \right) + \bar{\boldsymbol{F}}^L \\ &= -\frac{1}{h_S}\nabla \cdot \mathsf{S} + \bar{\boldsymbol{F}}^L \end{aligned}$$

[5] This term can be balanced against radiation-stress to produce "wave set-up/down" [33]

$\mathbf{S}$ is precisely the radiation-stress tensor used in [28],[29].

2.3.2 Mean flow response, later stage

The equations that we have derived are not adequate to describe the eventual steady state of the wave-driven current, where wave forcing balances bottom friction. In order for the friction to make a non-negligible contribution, we have to suppose that $\overline{\boldsymbol{u}}$ is $O(a)$. However, the set-up $\overline{\Delta h}$ still has to be $O(a^2)$ in order to balance a vortex with $\bar{u}^L$ of $O(a)$ (by cyclostrophic balance). The continuity equation, now truncated at $O(a)$, is

$$\nabla \cdot (h_S \bar{\boldsymbol{u}}^L) \;=\; 0$$

and the momentum equation (compare with (2.27): we have one additional term, the advection of mean momentum, and use the fact that $\bar{\boldsymbol{u}}^L \approx \overline{\boldsymbol{u}}$)

$$\frac{\partial \bar{\boldsymbol{u}}^L}{\partial t} + (\bar{\boldsymbol{u}}^L \cdot \nabla)\bar{\boldsymbol{u}}^L \;=\; -\frac{1}{h_S}\nabla \cdot \mathbf{S} - B$$

By taking the curl and manipulating the mean momentum term we find that

$$\left(\frac{\partial}{\partial t} + (\bar{\boldsymbol{u}}^L \cdot \nabla)\right) \boldsymbol{q} \;=\; -\frac{1}{h_S}\nabla \times (\frac{1}{h_S}\nabla \cdot \mathbf{S} + B) \qquad (2.27)$$

where $\boldsymbol{q} \equiv \frac{\nabla \times \bar{\boldsymbol{u}}^L}{h_S}$.

With this justification, we will proceed to use shallow water with a rigid lid for our numerical model. The radiation stress term will be discussed further

in §3.1.1. For the remainder of this dissertation, unless otherwise specified, $h(x, y)$ will refer to the still-water depth of the fluid under consideration, i.e. we will drop the subscript S from h_S.

2.3.3 Representation of friction

Finally, we must approximate the term

$$B = \frac{c_f}{h_S}\overline{\boldsymbol{u}|\boldsymbol{u}|}$$

Suppose that we assume a simple sinusoidal wave structure over which to take the phase (or time) average,

$$\boldsymbol{u} = ac\sin\theta\frac{\boldsymbol{k}}{\kappa}$$

where $\theta \in [0, 2\pi)$, a is the non-dimensional amplitude (expressed as a fraction of the still water depth h_S), and $c = \sqrt{gh_S}$ is the phase speed. We wish to have an expression that (at a minimum) includes both the quadratic mean-flow friction and an approximation to the littoral friction produced by the oscillating waves interacting with the mean current (as in [28]). To find the latter, we make the assumption that

$$|\boldsymbol{u}'| \gg |\overline{\boldsymbol{u}}|$$
$$|\boldsymbol{u}'| \gg |\bar{\boldsymbol{u}}^L|$$

Then

$$\begin{aligned} |\overline{\boldsymbol{u}}+\boldsymbol{u}'|(\overline{\boldsymbol{u}}+\boldsymbol{u}') &= \sqrt{|\overline{\boldsymbol{u}}|^2+2\overline{\boldsymbol{u}}\cdot\boldsymbol{u}'+|\boldsymbol{u}'|^2}(\overline{\boldsymbol{u}}+\boldsymbol{u}') \\ &\approx |\boldsymbol{u}'|\left(1+\frac{\overline{\boldsymbol{u}}\cdot\boldsymbol{u}'}{|\boldsymbol{u}'|^2}\right)(\overline{\boldsymbol{u}}+\boldsymbol{u}') \end{aligned} \tag{2.28}$$

Because $\overline{\boldsymbol{u}}$ is already phase-averaged (i.e. constant in θ), $\overline{|\overline{\boldsymbol{u}}|\boldsymbol{u}'}=0$. However $\overline{|\boldsymbol{u}'|}=\frac{2}{\pi}u'_{max}$, where $u'_{max}=ac$ is the maximum orbital velocity of the waves. Then averaging (2.28), we find

$$|\boldsymbol{u}'|\left(1+\frac{\overline{\boldsymbol{u}}\cdot\boldsymbol{u}'}{|\boldsymbol{u}'|^2}\right)(\overline{\boldsymbol{u}}+\boldsymbol{u}') = \frac{2}{\pi}u'_{max}\overline{\boldsymbol{u}}\cdot\left(\boldsymbol{\delta}+\frac{\boldsymbol{kk}}{\kappa^2}\right) \tag{2.29}$$

$\boldsymbol{\delta}$ is the Kronecker delta. To complete the expression for friction that we will use in the numerical model, we include the quadratic friction directly induced by the mean flow, so that

$$\begin{aligned} B &= \frac{c_f}{h_S}\frac{2}{\pi}u'_{max}\overline{\boldsymbol{u}}\cdot\left(\boldsymbol{\delta}+\frac{\boldsymbol{kk}}{\kappa^2}\right)+\frac{c_f}{h_S}|\overline{\boldsymbol{u}}|\overline{\boldsymbol{u}} \\ &= \frac{c_f}{h_S}\frac{2}{\pi}u'_{max}\bar{\boldsymbol{u}}^L\cdot\left(\boldsymbol{\delta}+\frac{\boldsymbol{kk}}{\kappa^2}\right)+\frac{c_f}{h_S}|\bar{\boldsymbol{u}}^L|\bar{\boldsymbol{u}}^L+O(a^3) \end{aligned}$$

The final expression can be justified by the fact that $\overline{u}$ and $\bar{u}^L$ are $O(a)$ quantitities that differ by a correction of $O(a^2)$.

Chapter 3

Longshore currents in the surf zone

3.1 Radiation stresses due to surface gravity waves

It can be demonstrated that for a variety of waves in fluids, there is a flux of momentum present in excess of what would be there in the absence of waves. Although previously known for some cases[27], this fact was derived comprehensively by Longuet-Higgins and Stewart in a series of papers [30, 31, 32]. The authors also used the framework of radiation stress to explain oceanographic phenomena such as surf beats [32], wave set-up [33, 34], and longshore currents [28].

Following [34], we will define radiation stress as *the excess flow of momentum due to the presence of the waves.* In order to correctly model the mean flow changes that result from waves, we have to predict any radiation stress convergence or divergence (which, by conservation of momentum, would shift its momentum to the mean flow). Because the waves are horizontal, we will always define the radiation stress as a vertically averaged quantity.

In [34], the radiation stress for progressive waves in water of uniform depth is computed. We begin with waves propagating in the x direction, with surface elevation given by

$$\xi = a\cos(kx - \omega t)$$

where a is the amplitude of the waves, k is the wave number, and ω is the radial frequency. The depth of the water is h, and we define the z-axis so that the still surface of the water lies at $z = 0$. Then the velocity components are given by

$$\begin{aligned} u &= \frac{a\omega}{\sinh kh}\cosh k(z+h)\cos(kx - \omega t) \\ w &= \frac{a\omega}{\sinh kh}\sinh k(z+h)\sin(kx - \omega t) \end{aligned}$$

We now compute the radiation stress $\mathbf{S}_{xx}$ by averaging the u-momentum flux across a plane $x = C$ over one wave period, and subtracting the momentum

flux at rest:

$$\mathbf{S}_{xx} = \overline{\int_{-h}^{\xi} (p + \rho u^2) dz} - \int_{-h}^{0} p_0 dz$$

where p_0 is the hydrostatic pressure.

One may compute that to $O(a^2)$,

$$\begin{aligned} \mathbf{S}_{xx} &= \int_{-h}^{0} \rho \overline{(u^2 - w^2)} dz + \frac{1}{2} \rho g \overline{\xi^2} \\ &= E \left(\frac{2kh}{\sinh 2kh} + \frac{1}{2} \right) \end{aligned}$$

where $E \equiv \frac{1}{2} \rho g a^2$ is the energy density of the waves.

In shallow water, where the particle orbits are approximately straight lines (that is, $w = 0$) and the velocity is the same throughout the water column, we can write this as

$$\mathbf{S}_{xx} = h_S \overline{u^2} + \frac{1}{2} \rho g \overline{\xi^2}$$

We can also compute $\mathbf{S}_{xy}$ the flux of x-momentum across a plane $y = C$, $\mathbf{S}_{yx}$ the flux of y-momentum across a plane $x = C$, and $\mathbf{S}_{yy}$ the flux of y-momentum

across a plane $y = C$. We find

$$\begin{aligned} \mathsf{S}_{xy} &= 0 \\ \mathsf{S}_{yx} &= 0 \\ \mathsf{S}_{yy} &= \frac{1}{2}\rho g\overline{\xi^2} \end{aligned}$$

If the direction of propagation is at angle θ to the x-axis, the radiation stress is given by a coordinate transformation from the propagation frame of reference to the "true" coordinate system. Written in tensor notation and using the notation of §2.3, we conclude that

$$\mathsf{S}_{ij} = h_S\overline{u_i' u_j'} + \delta_{ij}\frac{g}{2}\overline{h'^2} \tag{3.1}$$

This is the definition that we will use for the remainder of this thesis.

3.1.1 A decomposition of radiation stress for steady surface waves

The following is due to Buhler and Jacobson [10].

The time tendency of psuedomomentum $\mathbf{p}$ is given by 2.27. The radiation stress tensor is defined by 3.1. Comparing these two equations, we see that

$$-\frac{1}{h_S}\nabla\cdot\mathsf{S} = \frac{\partial \mathbf{p}}{\partial t} - \mathscr{F} - \frac{1}{2}\nabla\overline{|\boldsymbol{u}'|^2} \tag{3.2}$$

We can see that in the presence of steady waves, the only term with a non-zero curl (i.e. the only term that will force the mean vorticity) is $\mathscr{F}$.

By using the solution for the linear waves (2.26), we see that

$$\begin{aligned} \mathscr{F} &\equiv -\overline{\xi'_{j,i} \boldsymbol{F}'_j} \\ &= \boldsymbol{k}\omega^{-1}\overline{\boldsymbol{u}' \cdot \boldsymbol{F}} \end{aligned}$$

Using the equations satisfied by linear waves on resting fluid, we can show

$$\frac{\partial E}{\partial t} + \frac{1}{h_S}\nabla \cdot (g h_S \overline{h' \boldsymbol{u}'}) = \overline{\boldsymbol{u}' \cdot \boldsymbol{F}}$$

Furthermore, up to $O(a^2)$,

$$\bar{\boldsymbol{u}}^S = \mathbf{p} = \frac{\boldsymbol{k}}{\omega} E$$

With steady, monochromatic waves then,

$$\begin{aligned} \frac{\boldsymbol{k}}{\omega}\overline{\boldsymbol{u}' \cdot \boldsymbol{F}'} &= \frac{\boldsymbol{k}}{\omega}\frac{\partial E}{\partial t} + \frac{\boldsymbol{k}}{\omega h_S}\nabla \cdot (g h_S \overline{h' \boldsymbol{u}'}) && (3.3) \\ &= \frac{\boldsymbol{k}}{\omega h_S}\nabla \cdot (g h_S \overline{h' \boldsymbol{u}'}) && (3.4) \\ &= \frac{\boldsymbol{k}}{\omega h_S}\nabla \cdot (g h_S^2 \frac{\boldsymbol{k}}{\omega} E) && (3.5) \\ &= \frac{\boldsymbol{k}}{h_S}\nabla \cdot (h_S \frac{\boldsymbol{k}}{\kappa^2} E) && (3.6) \end{aligned}$$

3.2 Application to problem of longshore currents

A commonly used framework for predicting steady currents near the shore is by establishing a one-dimensional (in the cross-shore direction) momentum balance, wherein momentum flux due to radiation stresses must balance momentum flux due to bottom drag, wind stress, and/or turbulent mixing. This approach was used by Longuet-Higgins[28, 29].

Longuet-Higgins begins with the momentum equations for the shallow water equations: in particular the longshore momentum equation,

$$\frac{\partial v}{\partial t} + u\frac{\partial v}{\partial x} + v\frac{\partial v}{\partial y} = -c_f \frac{|\boldsymbol{u}|v}{h}.$$

Suppose that the flow consists of a mean flow added with a steady wave train, so that $v(x, y, t) = \langle v \rangle(x) + v'(x, y, t)$. The wave-train has a wave vector $\boldsymbol{k}$, which can be expressed in terms of its magnitude k and angle θ, where $\theta = 0$ indicates waves normal to the shore. At some point offshore the waves are characterized by phase speed c_0 and angle θ_0. We suppose that the shoreline is given by $x = 0$ as in 3.1. From the shoreline, the beach slopes monotonically downwards.

Averaging in time over a wave period (an operation we will denote by $\langle \cdot \rangle$),

we find

$$\frac{\partial}{\partial x}\langle hu'v'\rangle \;=\; \langle -c_f|\boldsymbol{u}|v\rangle$$

The first term in this balance is the convergence of radiation stress (assuming that u',v' are purely wave disturbances). However, small-scale turbulent motions may be present, and these may contribute to the flow of longshore momentum shoreward or seaward. Longuet-Higgins presumes that these effects will be well-modelled as an eddy diffusion of the mean velocity. He concludes that an acceptable model for the longshore momentum balance for the surf zone is

$$0 \;=\; -\frac{\partial \mathbf{S}_{xy}}{\partial x} + \frac{\partial}{\partial x}\left(N\frac{\partial\langle v\rangle}{\partial x}\right) - \langle c_f|\boldsymbol{u}|v\rangle \tag{3.7}$$

where N is some sort of parameterization of horizontal momentum flux. It is known ([30],§3.1) that the momentum flux *parallel* to the direction of propagation across any plane normal to the direction is given by

$$\mathbf{S}_{11} \;=\; E\left(\frac{1}{2} + \frac{2\kappa h}{\sinh 2\kappa h}\right)$$

and the momentum flux *perpendicular* to the direction of propagation is give

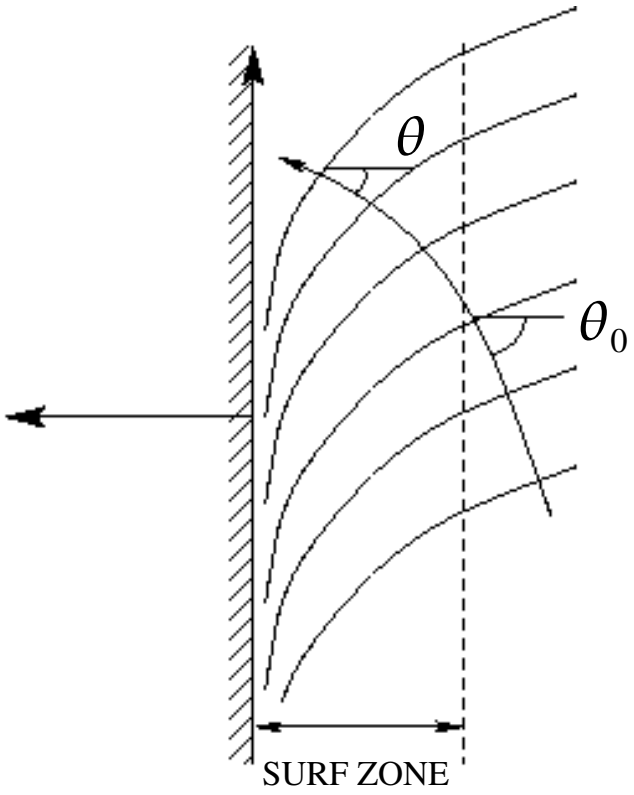

Figure 3.1: Schematic of shoreline in Longuet-Higgins' model (adapted from [28]). The "longshore" direction is along the y-axis (parallel to the shoreline) and the "cross-shore" direction is parallel to the x-axis

by

$$\mathbf{S}_{22} = E\frac{2\kappa h}{\sinh 2\kappa h}$$

where E is the wave energy per unit area, defined to be $E = \frac{1}{2}\rho g a^2$, where a is the amplitude (one half the distance from crest to trough) of the wave. By the standard coordinate transformation then, the flux of y momentum across a plane $x = c$ is given by

$$\begin{aligned} \mathbf{S}_{xy} &= E\frac{c_g}{c}\cos\theta\sin\theta \\ &= Ec_g\cos\theta\frac{\sin\theta_0}{c_0} \end{aligned} \tag{3.8}$$

using Snell's law.

In the absense of dissipation, the energy density E satisfies a conservation principle along rays; in its steady, longshore-homogeneous form, it is

$$\frac{\partial(Ec_g\cos\theta)}{\partial x} = 0$$

By comparison with 3.8, we see that $\mathbf{S}_{xy}$ changes with x if and when E is dissipated or generated.

In order to approximate $\frac{\partial \mathbf{S}_{xy}}{\partial x}$, we make the following assumptions. We suppose that waves break via saturation; when their height reaches a fraction of the local still water height, they are capped in a spilling breaker. Because the beach is sloping monotonically, and therefore undissipated waves slow and

shoal as they move shoreward, once a wave begins to break, it is capped at its saturation height until it reaches the shoreline. We additionally suppose that the waves are close enough to normal that $\cos\theta \approx 1$, and that $kh \ll 1$ so that $c_g \approx \sqrt{gh}$. Therefore we can approximate the wave amplitude and wave energy shoreward of the breaking line by

$$\begin{aligned} a &= \alpha h \\ \mathbf{S}_{xy} &= \frac{1}{2}\rho g(\alpha h)^2\sqrt{gh}\frac{\sin\theta_0}{c_0} \\ &= \frac{1}{2}\alpha^2\rho g^{3/2}h^{5/2}\frac{\sin\theta_0}{c_0} \end{aligned}$$

and

$$\begin{aligned} -\frac{\partial \mathbf{S}_{xy}}{\partial x} &= -\frac{5}{4}\alpha^2\rho(gh)^{3/2}\frac{\partial h}{\partial x}\frac{\sin\theta}{c} \\ &= -\frac{5}{4}\alpha^2\rho gh\frac{\partial h}{\partial x}\sin\theta \end{aligned}$$

Using the maximum horizontal orbital velocity from linear wave theory, wherein

$$u_{max} = \frac{a\sigma}{kh} = \alpha(gh)^{1/2}$$

this can be written as

$$-\frac{\partial \mathbf{S}_{xy}}{\partial x} = \frac{5}{4}\rho u_{max}^2\left(\frac{\partial h}{\partial x}\sin\theta\right)$$

We now turn to estimating the bottom friction.

$$B \equiv -c_f \rho |\boldsymbol{u}| v$$

The velocity in general is given by the sum of the orbital velocity u_{orb} and the average velocity $\langle v \rangle$. If the average velocity $\langle v \rangle$ is small compared to the orbital velocity, B is well approximated by the expression

$$\begin{aligned} \langle B \rangle &= c_f \rho \langle |u_{orb}| \rangle \langle v \rangle \\ &= \frac{2}{\pi} c_f \rho u_{max} \langle v \rangle \end{aligned}$$

assuming that u_{orb} is sinusoidal in time. If $\langle v \rangle$ is 0, however, the bottom friction, averaged over the orbital velocity, is 0.

We now return to the averaged momentum balance (3.7) and assume that "horizontal turbulence" is not present. Then balancing the radiation stress derivative and bottom friction, we find

$$\begin{aligned} \langle v \rangle &= \frac{5\pi}{8c_f} u_{max} \frac{\partial h}{\partial x} \sin\theta \\ &= \frac{5\pi}{8c_f} \alpha g h \frac{\partial h}{\partial x} \frac{\sin\theta}{c} \end{aligned}$$

This last equation makes it evident that when the local beach slope is constant, $\langle v \rangle$ is proportional to the local water depth. Seaward of the breaking line, the averaged bottom friction and the radiation stress convergence are 0, so the

momentum balance is satisfied trivially.

How do we generalize this argument to the case where the beach does not monotonically slope upwards (for example, the barred beach)? The difference is that as the wave travels into the deeper water of the bar trough, it will dip below saturation height. Because no significant dissipative processes are occuring, we can again take $\langle v \rangle = 0$ to be a consistent solution in this region. Therefore on a barred beach a current will be forced over the bar and close to the shoreline, the two locations where significant wave breaking occurs.

3.3 A mechanism for current dislocation

The one-dimensional momentum balance3.9 qualitatively reproduces current profiles on planar beaches. However, discrepancies have been noted on barred beaches [12, 13]. In particular, the local maximum of longshore current is moved or "dislocated" from the bar to the trough.

We propose a mechanism that will cause current dislocation on barred beaches, but not on planar beaches. This mechanism relies on understanding both the vorticity forced by breaking waves and the subsequent dynamics of regions of vorticity.

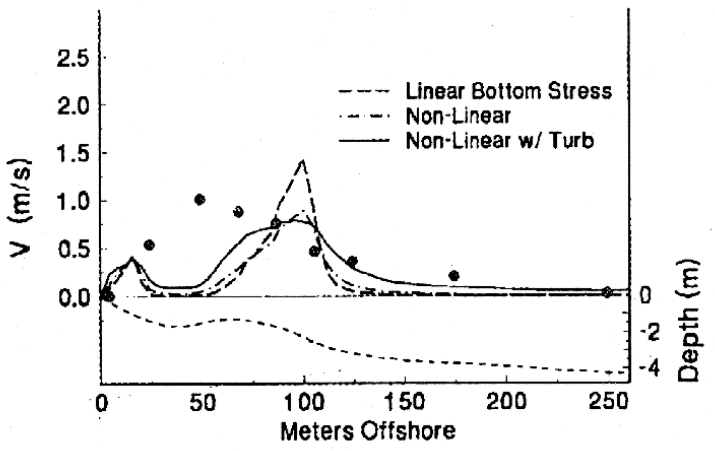

Figure 3.2: Mean currents (as solid dots) recorded at Duck, NC on Oct. 10, 1990 (from reference [12]

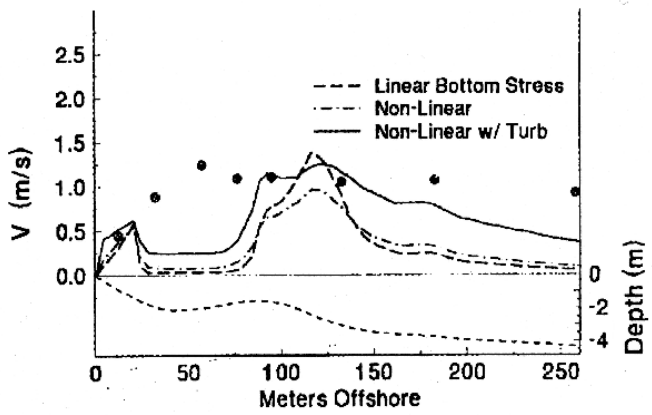

Figure 3.3: Mean currents (as solid dots) recorded at Duck, NC on Oct. 12, 1990 (from reference [12]

3.3.1 Inhomogeneous forcing/topography will force dipolar vortex structures

Suppose that a "packet"[1] of oblique waves advances on a beach (barred or planar). If the packet is supposed to break according to saturation, it will break when it reaches the appropriate height and impart some kind of longshore momentum to the current through the convergence of radiation stress. However, it will also impart vorticity to the flow. We can qualitatively assess the nature of this forcing by examining

$$-\frac{1}{h}\nabla\times\left(\frac{1}{h}\nabla\cdot\mathbf{S}\right)$$

which is the contribution that the radiation stress divergence makes to the vorticity evolution equation (2.27). In the case where both $\mathbf{S}$ and h are longshore homogeneous and $\theta > 0$, we find that this forcing takes the character of two "strips" of vorticity, one shoreward positive and one seaward negative. Together they force a longshore current in the expected direction, as we have already seen from the momentum perspective.

In the packet case, we find that this vorticity forcing takes the form of a dipole. There are several ways to see this result. From a fundamental fluid mechanical perspective, a wave that topples over and breaks introduces a topologically-induced circulation into the fluid when the wave rejoins the main body of water. Because the fluid is incompressible and largely inviscid,

[1] That is, the wavetrain is limited in longshore physical extent

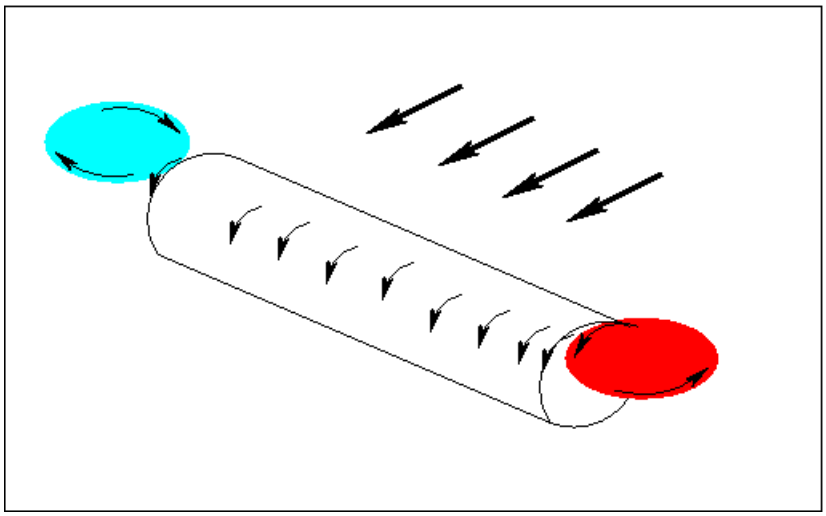

Figure 3.4: Schematic of bore showing circulation production on either end. The straight arrows indicate the direction of wave propagation (towards the shoreline)

vortex lines must reconnect or end on the surface of the fluid. In this case, the vortex lines must end at the surface at the edges of the breaking wave; the sense of the circulation produced at the leftward edge (from the perspective of an observer looking shoreward) is positive, at the rightward edge is negative (see figure 3.4).

From the model of a breaking wave as a bore, it has been demonstrated that the circulation produced around the edges of a bore of finite extent is proportional to the energy dissipation, but where the sign of the circulation depends on which edge is being considered[36]. Here, too, a dipole is justified.

3.3.2 Vortex dynamics can produce current dislocation

Now let us consider the vortex dynamics that take place on a sloping beach. Generally, I wish to refer in this discussion to isolated regions of vorticity. They can be characterized by their circulation

$$\begin{aligned} \Gamma &= \int\int_S hq \, dx \, dy \\ &= \int_{\partial S} \boldsymbol{u} \cdot dr \end{aligned}$$

where S is a simple region that contains the entire vortex region, and also by radius

$$b = \min_S \sqrt{\frac{1}{\pi} \int\int_S dx \; dy}$$

If the vortex is of circular shape, then b will give the actual radius.

There are several dynamical effects present that may effect the evolution of the vortices. The shallow water approximation assumes that there is no vertical variation in vorticity or velocity; therefore the usual two-dimensional vortex dynamics are active (see reference [11], Chapter 2). For example, two vortices of the same sign will tend to rotate about their center of circulation, and two vortices of opposing sign will tend mutually advect away, in a straight line if they are of equal magnitude.

There are also image vortices, necessitated by satisfying no-normal flow boundary conditions at any wall boundaries. A vortex that is near to a wall

will move along the wall as if a vortex of equal and opposite circulation were behind it[2].

Finally, we have a "self-advection" effect because of the sloping bottom. A region of positive or negative vorticity in a vorticity free region takes the form of a cylindrical shape. On a planar beach, a well-known approximation to this fluid motion is that of an axisymmetric vortex ring [27]. A vortex that takes the form of a circular arc will have motion identical to the corresponding vortex ring. The motion of a vortex ring may be characterized in terms of its circulation and inner and outer radii.

The velocity, according to [27], is given by

$$U = \frac{\Gamma}{4\pi R}\left(\ln\left(\frac{8R}{b}\right) - \frac{1}{4}\right) \tag{3.9}$$

Translated to the planar beach, the equivalent vortex ring has outer radius $h/|\nabla h|$ and inner radius b; due to mass conservation we must have

$$b = b_0\left(\frac{h_0}{h}\right)^{1/2}$$

throughout the motion of the vortex. Using these identities the self-advection velocity U (3.9) may be written in terms of these physical variables as

$$U = \frac{\Gamma}{4\pi}\left(\frac{\nabla h}{h}\times\hat{z}\right)\left(\ln\left(\frac{8}{b_0 h_0^{1/2}}\frac{h^{3/2}}{|\nabla h|}\right) - \frac{1}{4}\right) \tag{3.10}$$

[2]This is not exactly true if the wall is not straight; in this case the image vortex does not move according to ordinary vortex dynamics, but the effect on the "real" vortex is similar

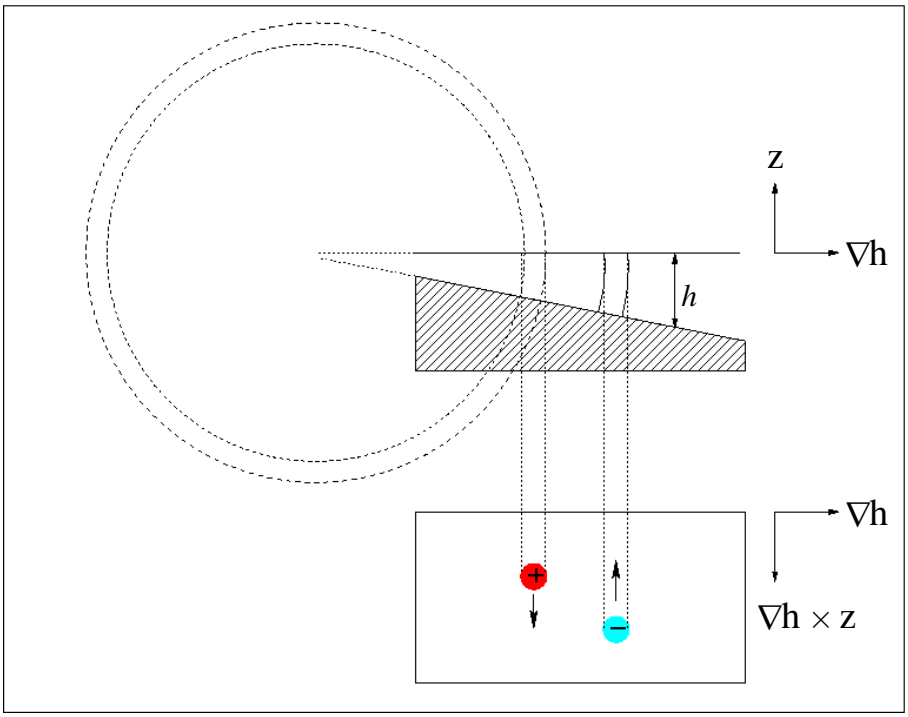

Figure 3.5: Self-advection on a planar beach

This makes clear that the direction of self-advection depends on both the circulation Γ and the direction of the gradient ∇h. The direction of "self-advection" is shown on 3.5. This approximation may also be used in the case of a non-planar beach, where the vortex ring is no longer an exact solution. We again use ∇h to determine the outer radius, but here it is a local slope. This expression 3.10 has been shown to be a leading order approximation [45] for the law of motion for vortices of small dimensionless radius $O(\epsilon)$, separated by distances of $O(1)$.

Together, these two facts explain why a packet of breaking waves will create

a dislocated current on a barred beach. First, a vortex dipole will be created at the location of the bar; or, on a planar beach, at the onset of breaking. The vortices by mutual advection will want to move shoreward. On a planar beach, self-advection will quickly move the vortices apart until their mutual advection is negligible.

On a barred beach, by contrast, the vortices will move closer together as they move shoreward. Therefore their shoreward motion is not arrested until the vortices climb out of the trough, separating now because the local slope of the topography has reversed[10]. The result is a dislocation of the corresponding alongshore momentum from the bar, the site of wave-breaking, to the trough, the eventual location of the vortices.

Chapter 4

Numerical Model

4.1 Vortical flow

We model the resolved vortical flow by the shallow water equations with a rigid lid in their velocity-stream formulation.

$$\begin{aligned} q &\equiv \frac{\nabla \times \boldsymbol{u}}{h} \\ \frac{Dq}{Dt} &= \frac{\nabla \times \boldsymbol{F}}{h} - \frac{c_f}{h} \nabla \times \left(\frac{|\boldsymbol{u}| \boldsymbol{u}}{h} \right) \end{aligned}$$

$\boldsymbol{u}$ is defined by the following equations

$$\begin{aligned} \nabla \cdot \left(\frac{\nabla \psi}{h} \right) &= hq \\ \boldsymbol{u} &= \frac{1}{h} \nabla^{\perp} \psi \end{aligned}$$

The domain is given to be

$$0 \leq x \leq D \tag{4.1}$$

$$0 \leq y \leq L \tag{4.2}$$

with boundary conditions

$$\begin{aligned} \psi(x,y) &= 0 \qquad x = 0 \\ \frac{\partial \psi}{\partial x}(x,y) &= M\psi(x,y) \qquad x = D \end{aligned}$$

and $\psi(x,y) = \psi(x,y+L)$. We have already seen that (see §2.2) given q, ψ and therefore $\boldsymbol{u}$ are uniquely determined.

We leave the determination of F for §4.2 and consider the numerical methods used to solve these equations.

First we consider the dynamic equation. We use grid-based rather than psuedo-spectral methods due to the arbitrary nature of the topography. At each time step, the Jacobian $J(\psi, q)$ is computed using the Arakawa Jacobian. The friction term is computed using second-order differences. The time integration is performed using the leapfrog method, with an occasional Huen predictor-corrector step (as in [35]) to control the computational mode. Because both the advection and the friction term are computed to second-order accuracy, we are satisfied to use a time discretization that is second-order as well.

A key consideration in these choices was the ability of the numerical scheme to preserve conservation of the kinetic energy and enstrophy (defined in §2.1). These conservation properties are believed to play a major role in constraining the spectral profile of a turbulent two-dimensional fluid, and so we do not believe we can perform a physically realistic turbulence simulation without them. The Arakawa Jacobian conserves discrete analogues of the energy and enstrophy, so that any change in these quantities (in the absence of forcing and dissipation) is due to time-stepping. With the time-stepping scheme used, we conserve the appropriate quantities with reasonable accuracy in simulations where sources of energy and enstrophy are absent. We were interested to find that alternative and popular time stepping schemes (leapfrog with a Robert-Asselin filter and the third-order Adam-Bashforth scheme) permitted an unacceptable decay of enstrophy, although energy was well conserved.

Two algorithms are used for the determination of ψ. The first, a direct inversion in Fourier space, allows very fast, non-iterative computation, but is limited to cases where $h(x, y) = h(x)$. The second is an iterative multi-grid solver that can be used for two-dimensional height fields (h depends on both x and y).

4.1.1 Direct inversion

We consider the Fourier transform in y

$$\hat{\psi}_k(x) \quad = \quad \int_0^L \psi(x, y) e^{-i\frac{2\pi k}{L}} dy$$

Then $\hat{\psi}_k$ solves the ordinary differential equation

$$\begin{aligned} \frac{\partial}{\partial x}\left(\frac{\partial \hat{\psi}_k}{\partial x}\right) - \left(\frac{2\pi k}{L}\right)^2 \frac{\hat{\psi}_k}{h} &= h\hat{q}_k \\ \hat{\psi}_k(0) &= 0 \\ \hat{\psi}_k(D) &= M\hat{\psi}_k(D) \end{aligned}$$

It remains to specify M, the Dirichlet-to-Neumann map.

Suppose that the topography is flat outside of the computational domain, i.e. $h(x, y) = 1$. Then the solution in the exterior must satisfy

$$\frac{\partial}{\partial x}\left(\frac{\partial \hat{\psi}_k}{\partial x}\right) - \left(\frac{2\pi k}{L}\right)^2 \frac{\hat{\psi}_k}{h} = 0$$

A general solution to this equation is given by

$$\hat{\psi}_k = C_1 e^{\frac{2\pi k x}{L}} + C_2 e^{-\frac{2\pi k x}{L}}$$

for $k \neq 0$, and

$$\hat{\psi}_0 = C_1 + C_2 x$$

if $k = 0$.

If ψ is to remain bounded as $x \to \infty$, then each Fourier component must

remain bounded; so for each $k \neq 0$ we have the requirement that

$$\hat{\psi}_k = C_2 e^{-\frac{2\pi k x}{L}}$$

and

$$\hat{\psi}_0 = C_1.$$

We can express this is a relationship between the Dirichlet and Neumann data on the boundary as

$$\frac{\partial \hat{\psi}_k}{\partial x}(D) = -\frac{2\pi k}{L}\hat{\psi}_k(D)$$

for $k \neq 0$, and

$$\frac{\partial \hat{\psi}_0}{\partial x}(D) = 0.$$

These conditions are easily incorporated into a finite difference stencil along with (4.3).

This is the simplest, but hardly the only model for the topography outside the boundary. As one alternative we may take the height field outside the domain to vary linearly with distance from the shoreline ($h(x) = \alpha(x - x_0)$),

so that

$$\frac{\partial^2 \hat{\psi}_k}{\partial x^2} - \frac{1}{x - x_0}\frac{\partial \hat{\psi}_k}{\partial x} - \left(\frac{2\pi k}{L}\right)^2 \hat{\psi}_k = h\hat{q}_k$$

which has the general solutions

$$\begin{aligned}
\hat{\psi}_k &= C_1(x - x_0)I_1(\lambda(x - x_0)) + C_2(x - x_0)K_1(\lambda(x - x_0)), \qquad k \neq 0 \\
\hat{\psi}_0 &= C_1 + C_2(x - x_0)^2
\end{aligned}$$

where $\lambda \equiv \frac{2\pi k}{L}$, and I_1, K_1 are modified Bessel functions of the first and second kind respectively. Again, discarding the non-bounded solution and computing the relationship between Dirichlet and Neumann data, we see

$$\begin{aligned}
\frac{\partial \hat{\psi}_k}{\partial x}(D) &= -\lambda \frac{K_0(\lambda(D - x_0))}{K_1(\lambda(D - x_0))}\hat{\psi}_k(D), \qquad k \neq 0 \\
\frac{\partial \hat{\psi}_0}{\partial x}(D) &= 0
\end{aligned}$$

In our simulations, we choose to model the exterior topography as flat. Because vortex pairs are attracted to deep water, we thought a deep exterior topography might encourage vortices to leave the domain (and therefore open boundary conditions using a sloping exterior topography will resolve a flow less accurately than when using a flat exterior topography). Also, the computations are somewhat simpler. In practice, for wave-driven dissipative simulations (such as those meant to model the barred beach), the choice doesn't

make much difference.

4.1.2 Multi-grid solver

In the case that $h(x, y)$ is no longer solely a function of x, the above approach is no longer appropriate. The equation for ψ is discretized in two dimensions and solved by standard multi-grid methods [19]. The multi-grid technique is a response to the insufficiency of classical iterative methods for inverting large systems of linear equations. We will describe the philosophy briefly before addressing some concerns peculiar to our particular problem.

The equations to solve are

$$\begin{aligned} \nabla \cdot \left(\frac{\nabla \psi}{h} \right) &= hq \\ \psi(x, y, t) &= \psi(x, y + L, t) \\ \psi(0, y, t) &= 0 \end{aligned} \tag{4.3}$$

A seaward boundary condition remains to be specified. We will consider the following two boundary conditions

$$\begin{aligned} \psi(D, y, t) &= C(t) \\ \frac{\partial \psi}{\partial x}(D, y, t) &= M\psi(D, y, t) \end{aligned}$$

where $C(t)$ is specified by the time-tendency equation (2.8). This is an elliptic

equation

$$Lu = f$$

with Dirichlet or Dirichlet and Dirichlet-to-Neumann boundary conditions. It may be discretized into a system of n_l linear equations using finite differences

$$L_l u_l = f_l.$$

Given an initial guess at u_l^0, we define the Gauss-Seidel method to be, component-wise,

$$u_{l,i} = \left[\sum_{j=1, j \neq i}^{n_l} L_{l,ij} u_{l,j} - f_{l,i} \right] / L_{l,ii}$$

Each $u_{l,i}$ is replaced as it is generated. Therefore the result depends on the ordering of equations.

For our problem, we define L_l to be the following symmetric, second-order finite-difference scheme. Let a grid be defined with spacing h_l in both the x

and y directions. Define

$$\begin{aligned} p_{i+} &= \frac{1}{h(x_i + h_l/2, y_j)} \\ p_{i-} &= \frac{1}{h(x_i - h_l/2, y_j)} \\ p_{j+} &= \frac{1}{h(x_i, y_j + h_l/2)} \\ p_{j-} &= \frac{1}{h(x_i, y_j - h_l/2)} \end{aligned}$$

$$\begin{aligned} L_l u_l(i,j) &= h_l^{-2}[p_{i+}u_{l,i+1\,j} + p_{i-}u_{l,i-1\,j} + p_{j+}u_{l,i\,j+1} \\ &+ p_{j-}u_{l,i\,j-1} - (p_{i+} + p_{i-} + p_{j+} + p_{j-})u_{l,ij}] \\ f_l(i,j) &= h(x_i, y_j)q(x_i, y_j) \end{aligned}$$

We take the ordering of equations in the Gauss-Seidel ordering to be the standard red-black ordering. In addition, we must define a prolongation operator $\mathscr{P}$ and a restriction operator $\mathscr{R}$ such that

$$\mathscr{P} : \mathscr{U}_{l-1} \to \mathscr{U}_l \tag{4.4}$$

$$\mathscr{R} : \mathscr{U}_l \to \mathscr{U}_{l-1} \tag{4.5}$$

$$\tag{4.6}$$

where $\mathscr{U}_l$ is the set of vectors of dimension n_l. We will construct a sequence of grids such that $h_{l-1} = 2h_l$.

The two-stage multi-grid algorithm

For the problem with Dirichlet boundary conditions and red-black ordering, it can easily be seen that the Gauss-Seidel method will convergence. However the speed of convergence is unacceptably slow; while it is efficient at reducing high-frequency errors, smooth errors will decay very slowly. We address this problem by combining Gauss-Seidel (or Jacobi, etc.), with a step that reduces smooth errors.

Suppose we generate an intermediate solution $\tilde{u}$ by smoothing on the grid h_l. We will refer to the smoothing operation consisting of ν Gauss-Seidel (or Jacobi) iterations by $\mathscr{S}_l^\nu$. We compute the defect

$$\begin{aligned} \tilde{u}_l &= \mathscr{S}_l^\nu u_l \\ d_l &= L_l \tilde{u}_l - f_l, \end{aligned}$$

and then restrict the defect onto the coarse grid and solve

$$\begin{aligned} d_{l-1} &= \mathscr{R}(d_l) \\ L_{l-1} v_{l-1} &= d_{l-1}. \end{aligned}$$

If this equation has been solved by direct inversion, its cost will have been reduced by 2^{3d}-fold, where d is the physical dimension of the problem. If it has been solved by smoothing, the smooth components will be more quickly reduced on this coarser grid. We restrict the defect rather than the intermediate

solution $\tilde{u}_l$ for the following reason; while $\tilde{u}_l$ may contain high-frequency components, which cannot be adequately resolved on the coarse grid, d_l contains only the remaining smooth errors.

Finally, we interpolate v_{l-1} onto the fine grid and correct the intermediate solution

$$\begin{aligned} v_l &= \mathscr{P}(v_{l-1}) \\ u_l^{new} &= \tilde{u}_l - v_l. \end{aligned}$$

In practice, this procedure is recursively called on a sequence of grids ($l = 0..m$,where 0 is the coarsest). We can write the algorithm as follows, in FORTRAN pseudo-code:

recursive subroutine mgm(l,u,f)

$$\begin{aligned} \bar{u}_l &= \mathscr{S}_l^{\nu_1} u_l \\ v &= 0 \\ \bar{u}_l^{new} &= \bar{u}_l - \mathscr{P}(L_{l-1}^{-1}(\mathscr{R}(L_l \bar{u}_l - f_l))) && l = 1 \\ &= \bar{u}_l - \mathscr{P}(\mathbf{mgm}(l-1, v, \mathscr{R}(L_l \bar{u}_l - f_l))) && l > 1 \\ u_l^{new} &= \mathscr{S}_l^{\nu_2} \bar{u}_l^{new} \end{aligned}$$

end subroutine

The interior correction step can also be repeated γ times. For $\gamma = 1$, this

is called a "V-cycle", for $\gamma = 2$ a "W-cycle".

Boundary conditions

Two different seaward boundary conditions are implemented: Dirichlet, in which $C(t)$ is specified by the time evolution equation (2.8), and Dirichlet-to-Neumann, in which the equation (2.9) must be satisfied at the seaward boundary. The Dirichlet condition is incorporated into the scheme in the usual way, by including the condition $\psi = C(t)$ as a forcing on the right hand side of the grid points immediately to the left of the boundary. The DtN condition is also incorporated into the finite difference scheme, as described in the next section.

Convergence

Because the multi-grid solver is used hundreds or thousands of times during a simulation (at each time step, which may be a fraction of a second), we wish to confirm that we will have a convergent algorithm for our problem for any input, and desirable to estimate or increase the rate of convergence.

For open boundary conditions, the Dirchlet-to-Neumann map that must be satisfied at the seaward boundary is given by (2.9). If we approximate the

expression by a truncated sum, we have

$$\begin{aligned} M_K\psi(D_H, y) &= \frac{1}{L}\sum_{0}^{K}\left[-\frac{4\pi k}{L}\left[\int_0^L \psi(D_H, t)cos(\frac{2\pi k}{L}(y-t))\right]\right] \\ &= \frac{1}{L}\left[\int_0^L \psi(D,t)\sum_{k=0}^{K}\left[-\frac{4\pi k}{L}\cos(\frac{2\pi k}{L}(y-t))\right]dt\right] \end{aligned}$$

In order to guarentee convergence, it will be sufficient to show the following facts: the $L_l = L_l^* > 0$ and $D_l > 0$, where D_l is the main diagonal of L_l and $A > 0$ means positive-definite.

We first incorporate the boundary condition into L_l. We can discretize this integral using any standard quadrature scheme, such as Simpson's 1/3 rule.

$$\frac{\psi(D+\Delta x, y) - \psi(D-\Delta x, y)}{2\Delta} = \left[\sum_{i=1}^{N}\Delta t\,(1+\text{mod }(i,2))\,\frac{1}{3}\psi(D, i\Delta t)\sum_{k=0}^{K}\left[-\frac{4\pi k}{L^2}\cos\left(\frac{2\pi k}{L}(y-i\Delta t)\right)\right]\right]$$

By also using the 5-point stencil applied at the boundary point, we can get rid of the exterior point and get the following equation ($p = \frac{1}{h}$, assuming that

$h = 1$ on the boundary):

$$\begin{aligned}
&\left(1 + p(D - \frac{\Delta x}{2}, y)\right)\psi(D - \Delta x, y) + \\
&\psi(D, y - \Delta y) + \\
&\psi(D, y + \Delta y) + \\
&-\left(3 + p(D - \frac{\Delta x}{2}, y)\right)\psi(D, y) + \\
2\Delta x &\left[\sum_{i=1}^{N} \Delta t\,(1 + \text{mod }(i, 2))\,\frac{1}{3}\psi(D, i\Delta t)\sum_{k=0}^{K}\left[-\frac{4\pi k}{L^2}\cos\left(\frac{2\pi k}{L}(y - i\Delta t)\right)\right]\right] = 0
\end{aligned}$$

This is an equation for $\psi(D, y)$. We notice that for two points on the boundary, the equations are symmetric; the coefficient in the stencil only depends on the distance between them. It is also true that the coefficients sum to zero. It remains to show that there is symmetry in the coefficients between boundary points ($x = D$) and their neighbors ($x = D - \Delta x$). So far, it is not true; but suppose that $h(D - \Delta x, y) \equiv h(D - \Delta x)$, which we can always have by enlarging the computational domain slightly. Then we can multiply each boundary equation by the factor

$$\frac{p(D - \frac{\Delta x}{2})}{1 + p(D - \frac{\Delta x}{2})}$$

to enforce symmetry. Since the factor is the same for each equation, we don't disturb the symmetry of coefficients between boundary points.

To show positive definiteness, we apply the Gershgorin Circle theorem [21]. By symmetry of L all eigenvalues are real. In order to show that all eigenvalues

are positive it is sufficient to show that all Gershgorin circles lie in the right-hand plane, and that at least one of them is isolated from zero. The matrix L contains one row for each point that is not fixed; it includes all interior points (including the y boundary points, where there is periodicity), and the right boundary. For every point *except* on the right boundary, the row is a standard finite difference stencil for the variable-coefficient Laplacian; in particular, the elements of the row sum to zero for interior points. Their Gershgorin circles lie in the right-hand plane but include zero on their boundary. As pointed out earlier, this is also true for right-hand boundary equations. However, the Gershgorin circles corresponding to points next to the left hand boundary do *not* include zero. Because zero is on the boundary of the union of Gershgorin circles, it cannot be an eigenvalue unless it is on the boundary of *all* Gershgorin circles.

The same fact holds for the finite difference matrix in which Dirchlet conditions have been used. The difference here is that the Gershgorin circles corresponding to the points next to the right-hand side boundary lie entirely in the right-hand plane. So again L must be positive definite because it cannot have 0 as an eigenvalue.

To prove that the multi-grid algorithm with our choice of construction is convergent, we appeal to the arguments in reference [4]. While there are many other proofs of similar results [19, 59], the summary we will give below has the advantage of being entirely algebraic and so refers directly to the linear system being solved.

In [4], Banks and Douglas obtain estimates for the spectral radius of the iteration matrix associated with the multi-grid algorithm; that is, the convergence rate of one step of the iteration. Let L be the matrix of coefficients of the discretized PDE problem (we have dropped the subscript l used previously), and B be a matrix associated with a smoother, such that

$$Z^{j+1} = Z^j + B^{-1}(G - LW)$$

is equivalent to one step of the smoothing method.

In the formulation above the matrix equation that we wish to solve is

$$LZ = G \tag{4.7}$$

and B is the matrix associated with the symmetric Gauss-Seidel method,

$$B = (D - A)D^{-1}(D - A)^T$$

where A is the strictly lower triangular part of L; that is,

$$L = D - A - A^T$$

B is symmetric positive definite, as is L (from the previous argument). According to [4], that all of the generalized eigenvalues are positive is sufficient

for convergence. In particular, if there is κ such that

$$\sqrt{u^T B u} \leq \kappa^{1/2} \sqrt{u^T A u}$$

then various numerical values are proposed for the spectral radius of the iteration step. In particular, we can see that

$$\kappa = \lambda_{max}$$

is sufficient, where λ_{max} is the maximum eigenvalue of the generalized eigenvalue problem for A and B. The result of [4] is that for a single iteration of the multigrid algorithm, the error is decreased by a factor of

$$\gamma \quad = \quad \frac{\kappa}{\kappa + m}$$

where m is the number of smoothing iterations used.

However, this is a very, very pessimistic bound. The actual condition specified in the theorems in this paper refers to the ratio of $u^T B u$ to $u^T A u$ on the subspace $M_{j-1}^{\perp} \cap M_j$.

To give examples demonstrating the convergence rate, we show three inversion cases. We examine $\| L\psi - hq \|_{L^2}$, the L^2 error of the residual. Each vorticity field is chosen from a simulation, and inverted using the multi-grid algorithm, with a tolerance $\| L\psi - hq \|_{L^2} < 10^{-8}$. The rate of decrease of the residual is very similar for each case, with the residual decreasing by a factor

$10 - 12$ with each iteration.

4.2 Waves

The waves are modelled by a parameterization that resolves the rotational part of the momentum convergence of breaking waves. As we have observed in §2.3 the radiation stress tensor appears in our asymptotic description of the shallow water equations with small-amplitude waves, as a forcing on the averaged, vortical flow (2.27). The same expression was previously derived by Longuet-Higgins and Stewart ([34] and many others) as the excess momentum flux that occurs in the presence of waves. We begin from the point of view of §3.1.1, that

$$-\frac{1}{h_S}\nabla\cdot\mathsf{S} \;=\; \frac{\partial \mathbf{p}}{\partial t} - \mathscr{F} - \frac{1}{2}\nabla\overline{|\boldsymbol{u}'|^2} \tag{4.8}$$

If the waves are steady, we need only resolve

$$\mathscr{F} \;=\; \frac{\boldsymbol{k}}{h_S}\nabla\cdot(h_S\frac{\boldsymbol{k}}{\kappa^2}E).$$

This expression only depends on the steady wave train. We propose to compute the necessary fields by computation along ray trajectories. We will find this to be suitable for the saturation breaking criteria that we use to model wave breaking.

We begin by presenting the general theory of raytracing in nonhomoge-

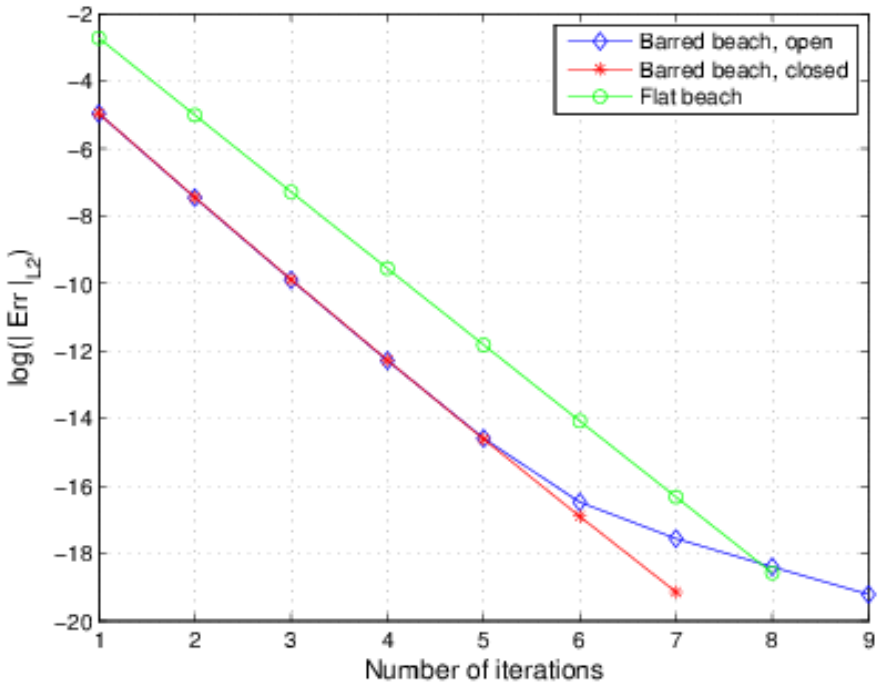

Figure 4.1: $\| L\psi - hq \|_{L^2} < 10^{-8}$ for the three example inversions shown in Figures 4.2,4.3,and 4.4.

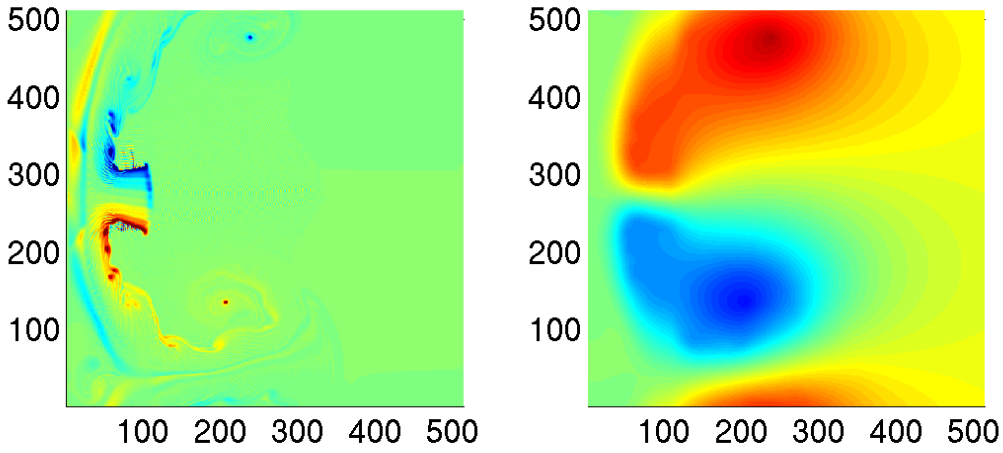

Figure 4.2: The vorticity field hq (left) and stream function ψ (right) for a barred beach with open boundary conditions.

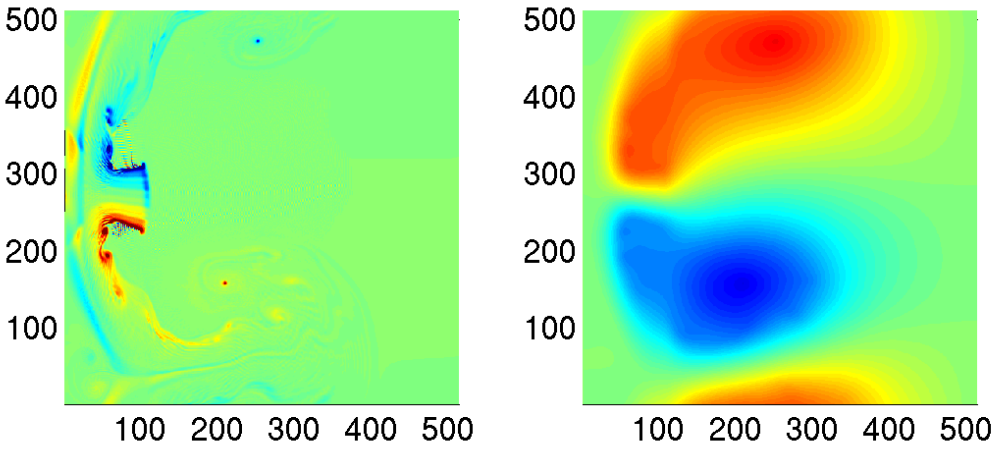

Figure 4.3: The vorticity field hq (left) and stream function ψ (right) for a barred beach with closed boundary conditions.

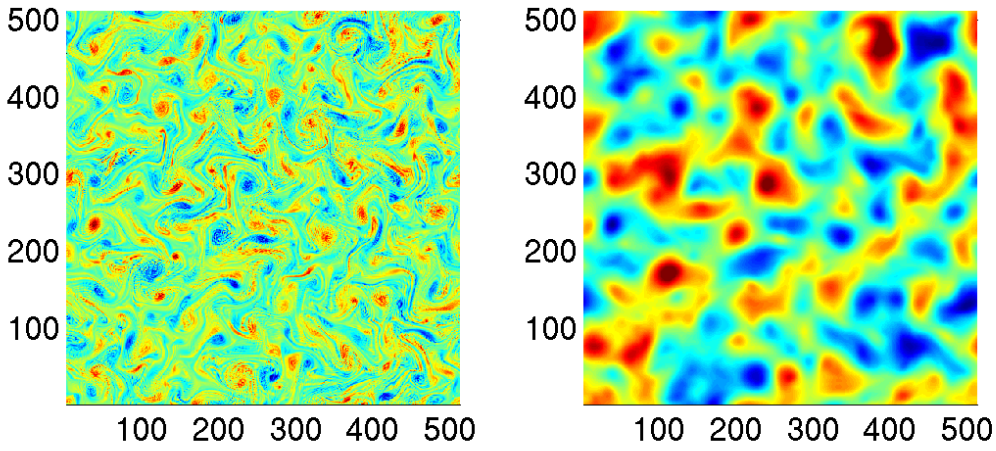

Figure 4.4: The vorticity field hq (left) and stream function ψ (right) for a flat beach with periodic boundaries.

neous, but slowly varying, dispersive systems. In addition we will assume that the background state is one of rest (otherwise a parallel development is possible). We consider the phase $\phi(x,t)$, and determines its evolution from

$$\omega(x,t) = -\frac{\partial \phi}{\partial t} \tag{4.9}$$

$$k(x,t) = \nabla\phi \tag{4.10}$$

We assume that ω is determined by a dispersion relation $\omega = \Omega(k,x)$. Then the characteristics of ϕ are given by

$$\begin{aligned} \frac{dx}{dt} &= \Omega_k \\ \frac{dk}{dt} &= -\Omega_x \end{aligned} \tag{4.11}$$

We define $c_g \equiv \Omega_k$ to be the *group velocity*. We see from (4.11) that the group velocity gives the speed of wave quantities in the propagation space.

It remains to compute the wave action per unit area, which in this case is given by $A = \omega E$ (again, because the waves are propagating on a background state of rest, there is no distinction between intrinsic and relative frequency).

The wave action per unit area A can be given by the so-called derived ray equations [20]:

$$\frac{d\nabla k}{dt} = -\nabla k \cdot \Omega_{kl} \cdot \nabla k - \Omega_{kx} \cdot \nabla k - \nabla k \cdot \Omega_{kx}^T - \Omega_{xx} \tag{4.12}$$

$$\frac{dlnJ}{dt} = \nabla k : \Omega_k + tr(\Omega_{kx}) \tag{4.13}$$

$$AJ = constant \tag{4.14}$$

where

$$\nabla k = \begin{bmatrix} k_x & l_x \\ k_y & l_y \end{bmatrix}$$

$$\Omega_{kx} = \begin{bmatrix} \omega_{kx} & \omega_{lx} \\ \omega_{ky} & \omega_{ly} \end{bmatrix}$$

and so forth.

J is the Jacobian determinant of x with respect to α, the initial origin of the rays. The law for the action is essentially a restatement of the fact that A is the density of a conserved quantity along wave trajectories in the absence of dissipation.

These equations will become singular if caustics or foci arise in the ray tracing. Essentially, the situation that we are faced with is that

$$\begin{aligned} \nabla \boldsymbol{k} &\rightarrow \infty \\ J &\rightarrow 0 \end{aligned}$$

While this can't arise in one-dimensional topography, it may happen for two-dimensional topography. It is advantageous to have a method for computing J which can be continued through a focus, if only so that we can detect them should they arise[1]. We use an alternative scheme proposed in [58]. Their solution is to propose an alternative set of equations that cleverly combine $\nabla \boldsymbol{k}$ and J into a variable that remains finite through a focus.

We begin by supposing that we begin with an initially plane wavefront at

[1]This would still not be sufficient to compute the action, however, because the law for action would not give an accurate description of the wave envelope in the vicinity of a focus.

a curve $\boldsymbol{x}_0(\alpha)$, parametrized by arclength α. Let

$$\gamma = (t, \alpha)^T$$

so that $\boldsymbol{x}_\gamma$ is the 2 x 2 matrix of derivatives of the transformation from ray coordinates (γ) to physical space. Let me define the unit tangent $\boldsymbol{e}_1$ along a ray

$$\boldsymbol{e}_1(t, \alpha) = \frac{\Omega_k(\boldsymbol{x}, \boldsymbol{k})}{|\Omega_k(\boldsymbol{x}, \boldsymbol{k})|}$$

and define $\boldsymbol{e}_2$ so that $\boldsymbol{e}_2 \perp \boldsymbol{e}_1$ and $(\boldsymbol{e}_1, \boldsymbol{e}_2)$ are right-handed. Given these definitions, the Jacobian of the transformation $(t, \alpha) \rightarrow \boldsymbol{x}$

$$\begin{aligned} J &= det(\boldsymbol{x}_\gamma) \\ &= |\Omega_k| \tilde{A} \end{aligned}$$

where $\tilde{A} \equiv \boldsymbol{e}_2^T \cdot \boldsymbol{x}_\alpha$ is the raytube area.

White and Fornberg now turn to the derived ray equation, written in matrix form here as

$$\frac{\partial}{\partial t}\boldsymbol{k}_x(\boldsymbol{x}(t, \alpha)) = -\Omega_{xx} - \Omega_{xk}\boldsymbol{k}_x - \boldsymbol{k}_x\Omega_{kx} - \boldsymbol{k}_x\Omega_{kk}\boldsymbol{k}_x$$

By changing to the $(\boldsymbol{e}_1, \boldsymbol{e}_2)$ basis and other manipulations, they show that

$$\begin{aligned}
\frac{\partial \tilde{A}}{\partial t} &= \mu_2 \tilde{A} + \mu_3 \tilde{B} \\
\frac{\partial \tilde{B}}{\partial t} &= \mu_1 \tilde{A} - \mu_2 \tilde{B}
\end{aligned}$$

where $B \equiv \tilde{A} \boldsymbol{e}_2^T \cdot \boldsymbol{k}_x \cdot \boldsymbol{e}_2$ and

$$\begin{aligned}
\mu_1 &= -\boldsymbol{e}_2^T \cdot \Omega_{xx} \cdot \boldsymbol{e}_2 + 2\frac{\boldsymbol{e}_2^T \Omega_x}{|\Omega_k|}\left[\boldsymbol{e}_1^T \cdot \Omega_{kx} \cdot \boldsymbol{e}_2 + \boldsymbol{e}_2^T \cdot \Omega_{kx} \cdot \boldsymbol{e}_1\right] \\
&\quad -2\left(\frac{\boldsymbol{e}_1^T \cdot \Omega_x}{|\Omega_k|}\right)\left(\frac{\boldsymbol{e}_2^T \cdot \Omega_x}{|\Omega_k|}\right)\boldsymbol{e}_1^T \cdot \Omega_{kk} \cdot \boldsymbol{e}_2 \\
&\quad -\left(\frac{\boldsymbol{e}_2^T \cdot \Omega_x}{|\Omega_k|}\right)^2\left[\boldsymbol{e}_1^T \Omega_{kk} \cdot \boldsymbol{e}_1 + 2\boldsymbol{e}_2^T \cdot \Omega_{kk} \cdot e_2\right] \\
\mu_2 &= -e_1^T \cdot \Omega_{kk} \cdot \boldsymbol{e}_2\left(\frac{\boldsymbol{e}_2^T \cdot \Omega_x}{|\Omega_k|}\right) + \boldsymbol{e}_2^T \cdot \Omega_{kx} \cdot \boldsymbol{e}_2 \\
\mu_3 &= \boldsymbol{e}_2^T \cdot \Omega_{kk} \cdot \boldsymbol{e}_2
\end{aligned}$$

While very dull to look at (and to write), these equations are very easy to implement and to solve numerically. They are linear equations and are solvable even if $\tilde{A}$ goes through 0.

The wave action per unit area, then, is easily computed in terms of $\tilde{A}$ and the local group velocity $|\Omega_k|$ in the absence of dissipation. If dissipation is present, we must model the process somehow; some models rely on a rate of energy dissipation along the ray trajectory, we use a saturation criterion. Either way, we wish to recover the *implicit* effect of wave dissipation by computing $\mathscr{F}$. Notice that for non-dispersive waves, including shallow water waves, we

can write

$$\begin{aligned} \mathscr{F} &= \frac{\boldsymbol{k}}{h_S}\nabla\cdot(c_g A) \\ &= \frac{\boldsymbol{k}}{h_S}D \end{aligned}$$

for $D \equiv \nabla\cdot(c_g A)$. Note also that in a steady wave train

$$\begin{aligned} D &= \frac{\partial A}{\partial t} + \nabla\cdot(c_g A) \\ &= \frac{dA}{dt} + (\nabla\cdot c_g)A \end{aligned} \tag{4.15}$$

However in the absence of dissipation, action conservation states that

$$\frac{dA}{dt} + (\nabla\cdot c_g)A = 0$$

Let us approximate both (4.15) and (4.16) by the Euler method along a trajectory:

$$\begin{aligned} A_{t+\Delta t}^{undisp} - A_t + (\nabla\cdot c_g)A_t\Delta t &= 0 \\ A_{t+\Delta t}^{disp} - A_t + (\nabla\cdot c_g)A_t\Delta t &= D\Delta t \end{aligned}$$

Consequently

$$D = \frac{1}{\Delta t}(A_{t+\Delta t}^{disp} - A_{t+\Delta t}^{undisp})$$

This equation may be used in two ways; if a waves "saturates" - that is, it breaks when it reaches an unstable amplitude - then A^{disp} is known and D can be solved for. If instead a model is given for D, then A^{disp} is recovered. A^{undisp} is always given by action conservation from the previous "time" step.

4.2.1 Dissipation models

Saturation

We employ for most of our simulations the following saturation criterion: if as the wave travels towards the shore, its height H exceeds a fraction α of the still water depth, it will "break" and be forced to maintain the saturation amplitude. We take $\alpha = 0.41$ and define H to be the maximum displacement from the still water depth (one half the vertical distance from crest to trough).

Dissipation incorporating randomness

In order to test the robustness of our results we also use a model for wave dissipation in [46]. A breaking wave is assumed to have a rate of energy dissipation equal to that of a bore whose shallow water depth is given by the still water depth h, and the deep water height is given by the height still water depth plus the wave height H [5]; assuming that H is proportional to the water depth, we arrive at a function of the wave energy, with C still to be

determined,

$$\begin{aligned} D_b &= \frac{C}{4}\rho g\omega\frac{H^3}{h} \\ &= \frac{C}{4}\rho g\omega h^2 \\ &= 2C\omega E. \end{aligned}$$

Then, a wave has some probability of breaking; this function is given with reference to a reference energy E_{ref}

$$P_b = \left[1 - e^{-\left(\frac{E}{E_{ref}}\right)^{(n/2)}}\right]$$

This function has the character of an "on-off" function, with P_b being close to 1 for $E > E_{ref}$, and close to 0 for $E < E_{ref}$. The sharpness of the transition increases as n increases. In our simulation, we let E_{ref} be the energy corresponding to a wave of saturation height $H = \alpha h$. Put together, the energy dissipation rate of a wave progressing towards the shoreline is given by

$$P_b D_b = \left[1 - e^{-\left(\frac{E}{E_{ref}}\right)^{(n/2)}}\right] 2C\omega E$$

Waves the evolve using this dissipation model differ from those that break according to the saturation model in several ways. Waves are now allowed to exceed the saturation threshold, although they will quickly be damped down. The main effect of this different concept of evolving wave energy is to shift

the location of wave dissipation; dissipation is no longer limited to regions of upward sloping topography. In particular, on the barred beach, dissipation is shifted "forward" onto the shoreward side of the bar (see figure (4.5)).

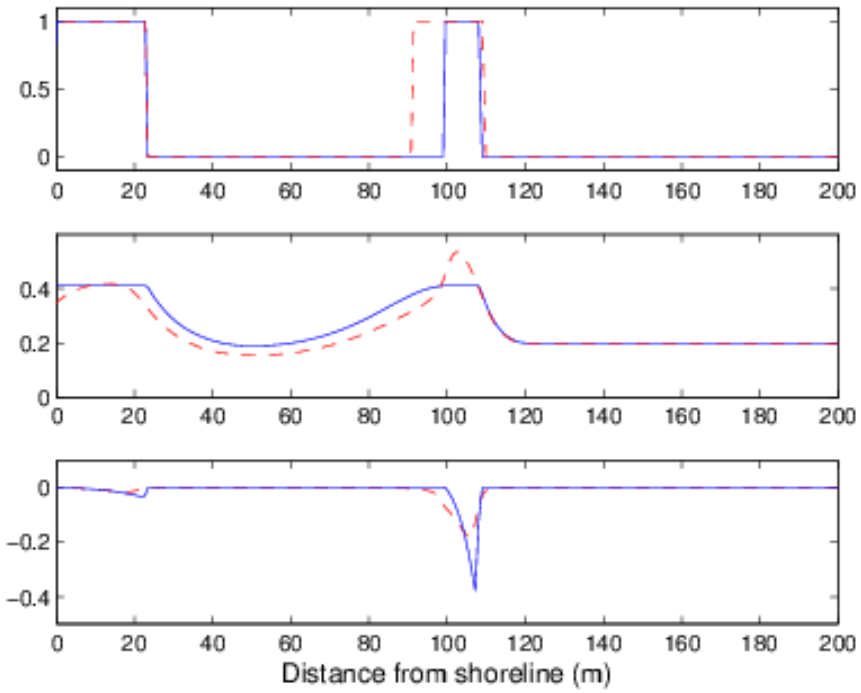

Figure 4.5: Breaking flag (top), non-dimensional amplitude, as fraction of still water depth (middle), and magnitude of dissipation (bottom) for both saturation (blue solid) and random (red dashed) wave dissipation models.

Chapter 5

Current dislocation in an idealized numerical experiment

We first demonstrate an idealized experiment that shows the current dislocation can occur when, as predicted, longshore inhomogeneity in wave structure or topography is present. This experiment is modelled on simulations presented in [10] with a non-linear shallow water model. The simulations are run for a total of 10 hours, simulation time, starting from rest. A constant forcing resulting from wave-breaking parameterization is applied. The waves are either assumed to come in from the sea with no alongshore variation, or in a Gaussian-shaped packet, whose length is 3 times the wavelength. The parameters that are varied between simulations are topography and wave packet structure. The time step is variable and is set so that the CFL, defined in reference to the maximum (resolved current) velocity, is within an appropriate

range ($< .9$).

Two types of topography are considered, a planar beach and a barred beach as used in [10]. We should find that current dislocation will occur when inhomogeneity in the longshore direction permits the creation of strong vortex dipoles during wave breaking. Furthermore, the degree of dislocation will depend on the shape of the topography, as vortex dynamics will govern the newly formed dipole.

Parameter	Definition	Formula or value
CFL	Courant-Friedrichs-Levy number	< 0.9
Δt	Time step	$\frac{CFL}{\max \lvert\mathbf{u}\rvert} \frac{1}{1/\Delta x + 1/\Delta y} s$
Δx	x (cross-shore)-grid spacing	$1\,m$
Δy	y (alongshore)-grid spacing	$1\,m$
D	Cross-shore dimension	$512\,m$
L	Alongshore dimension	$512\,m$
h_{S_0}	Still-water depth at seaward boundary	$4\,m$
a	Amplitude of waves at seaward boundary	$0.2\,h_{S_0}$
θ	Angle of incidence at seaward boundary	15
κ	Magnitude of wave-number vector	$0.29\,m^{-1}$
λ	Wave-length	$2\pi/\kappa$

Table 5.1: Parameters common over simulations A,B,C,D

Simulations D and B then (homogeneous forcing and homogeneous to-

Simulation	Topography	Wave packet structure	c_f
A	Barred	Packet	0.01
B	Barred	Homogeneous	0.01
C	Linear	Packet	0.01
D	Linear	Homogeneous	0.01

Table 5.2: Description of simulations

pography) should show no current dislocation and should broadly satisfy the predictions of [28, 29]. Simulation C (inhomogeneous wave forcing, but planar beach) should show modest dislocation, because the topography is not conducive to forward motion of vortices. Simulation A should show marked dislocation, with a preference for the local maximum of water depth.

The forcing profiles for each simulation clearly show the expected dipole pattern when predicted.

The early development of current is as expected. For homogeneous waves breaking on a barred beach (simulation B), the current develops over the bar, where its maximum is located for the entirety of the simulation. On a planar beach, the current initially develops at the location of wave breaking and shows a slight shift shoreward as the simulation progresses, consistent with the vortex dynamics. On a barred beach, the current initially develops on the bar, but shows a marked shift shorewards as the simulation progresses, with its maximum located at the bar trough.

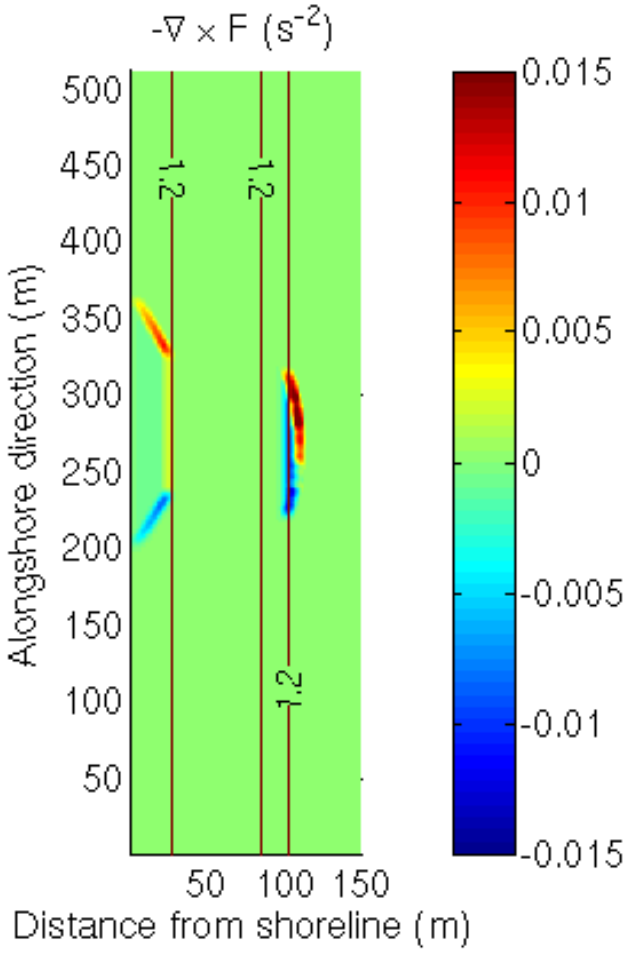

Figure 5.1: $-\nabla \times F$ for simulation A

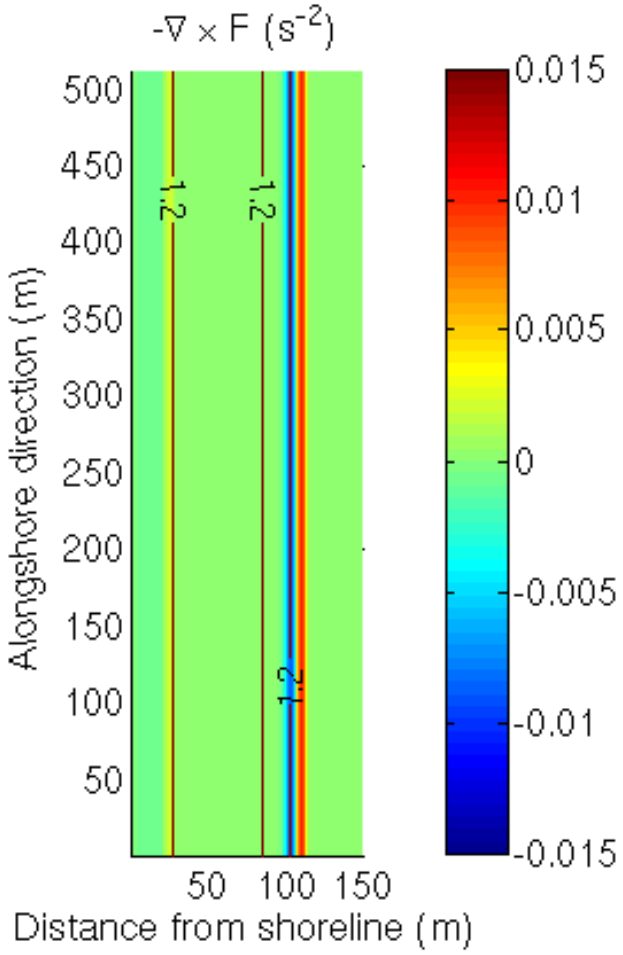

Figure 5.2: $-\nabla \times F$ for simulation B

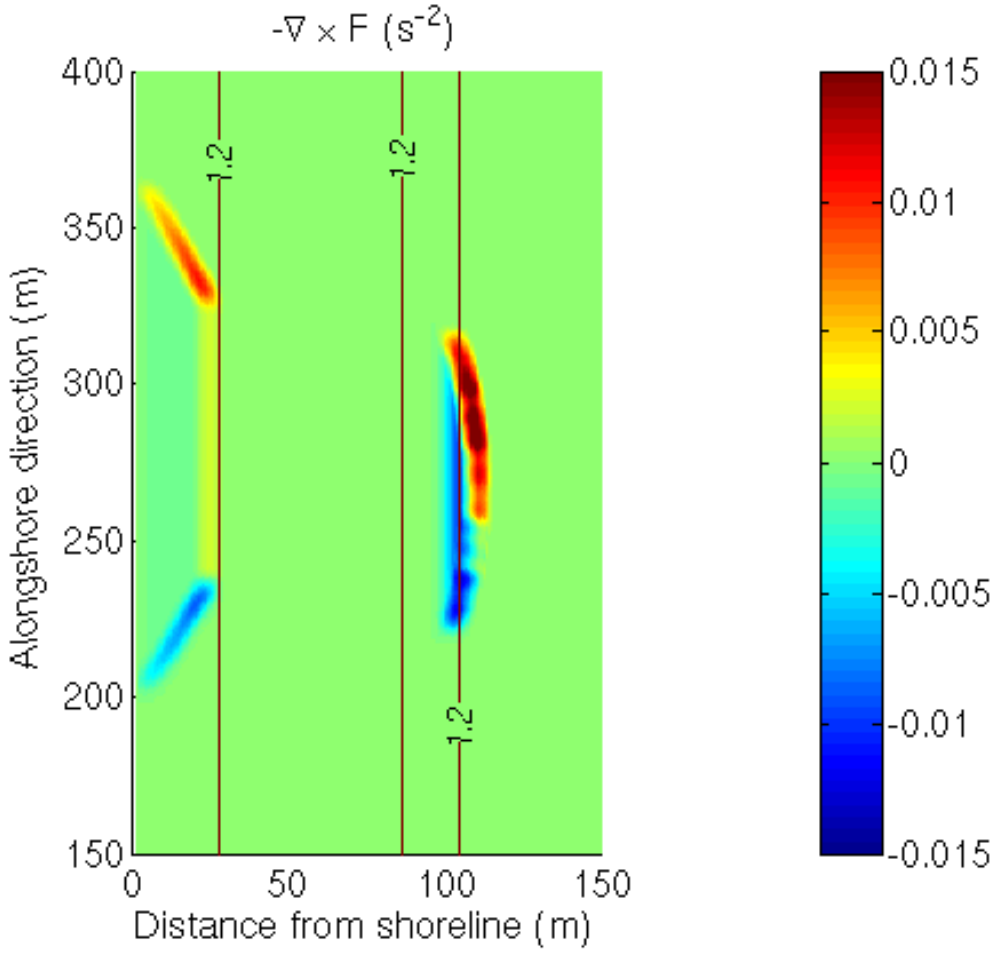

Figure 5.3: Closeup of $-\nabla \times F$ for simulation A

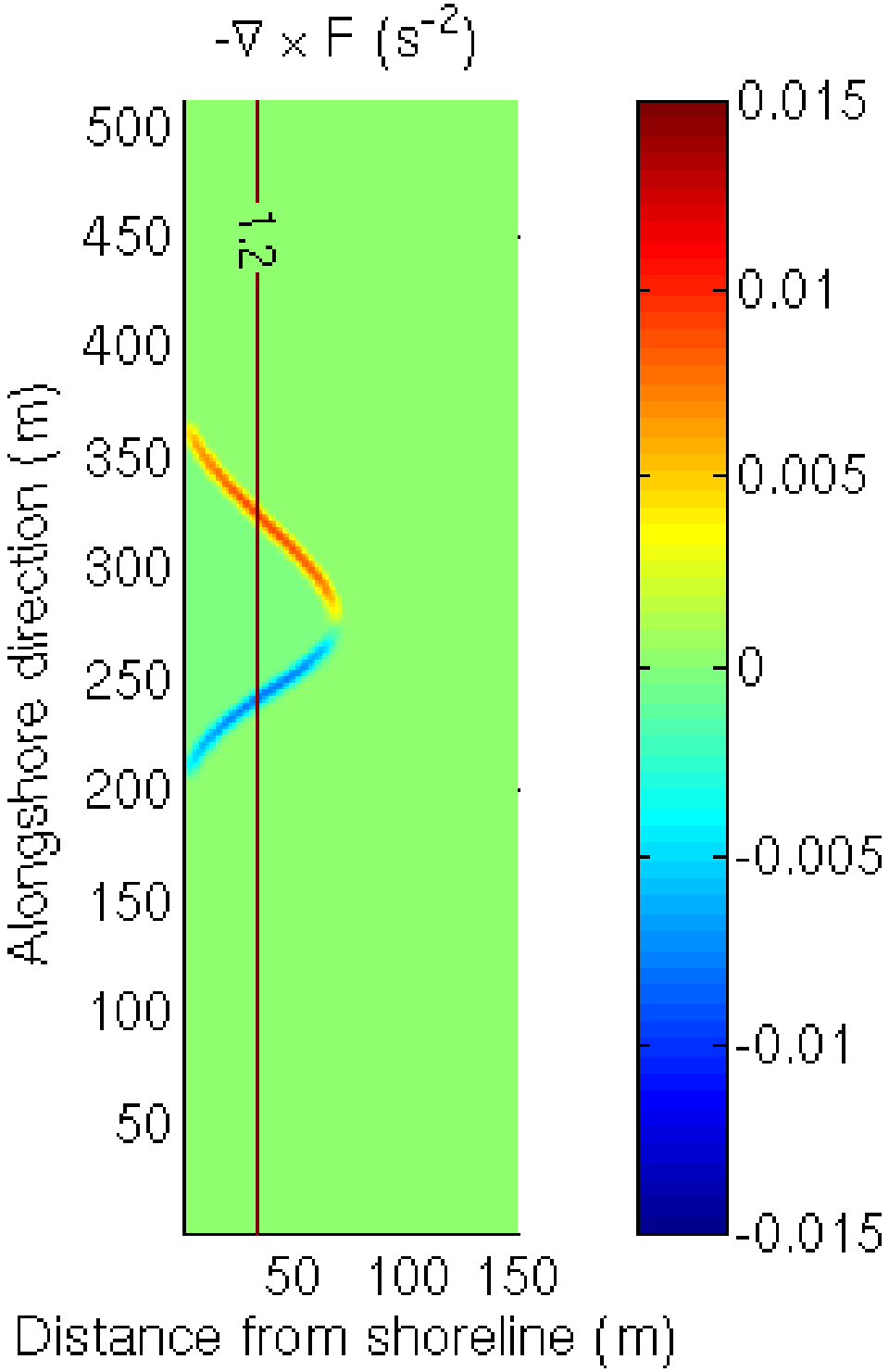

Figure 5.4: $-\nabla \times F$ for simulation C

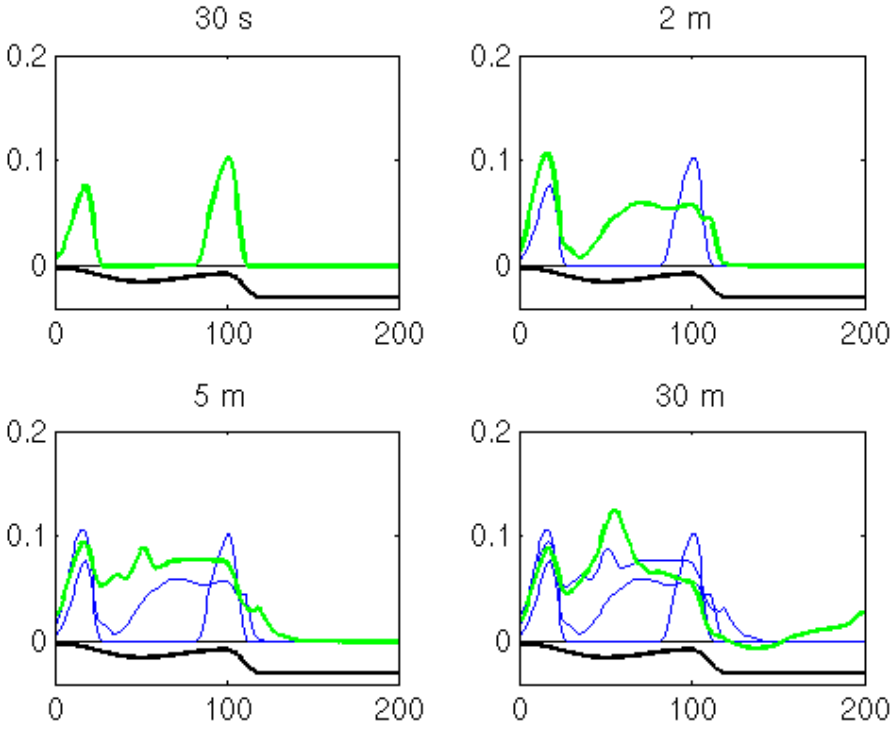

Figure 5.5: Early development of mean longshore current for simulation A

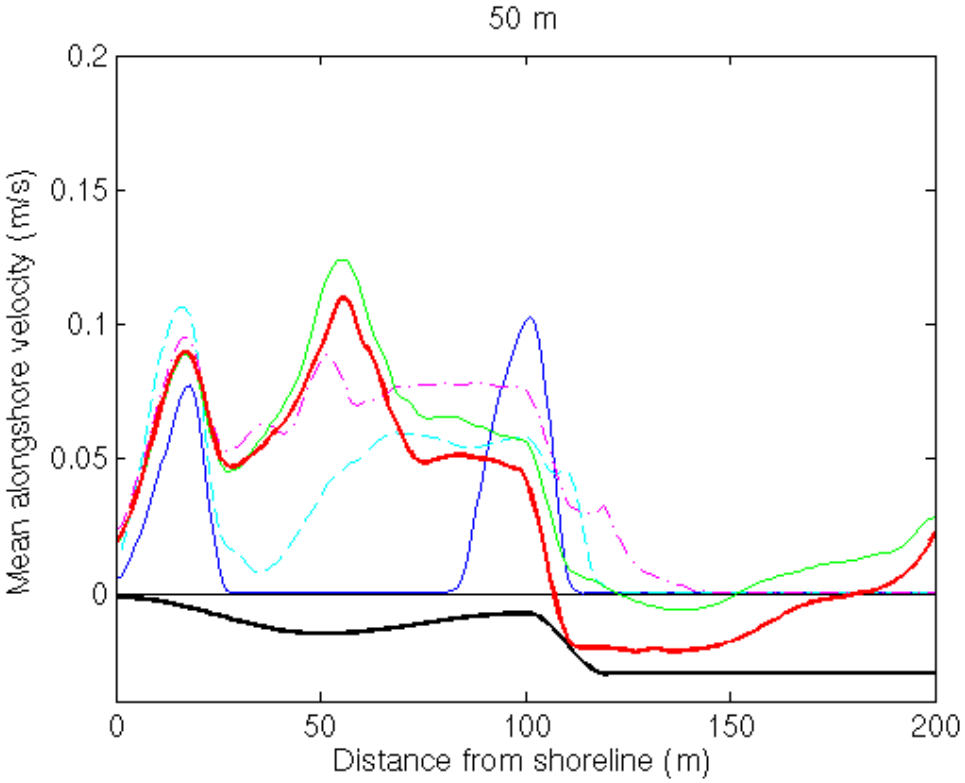

Figure 5.6: Early development of mean longshore current for simulation A

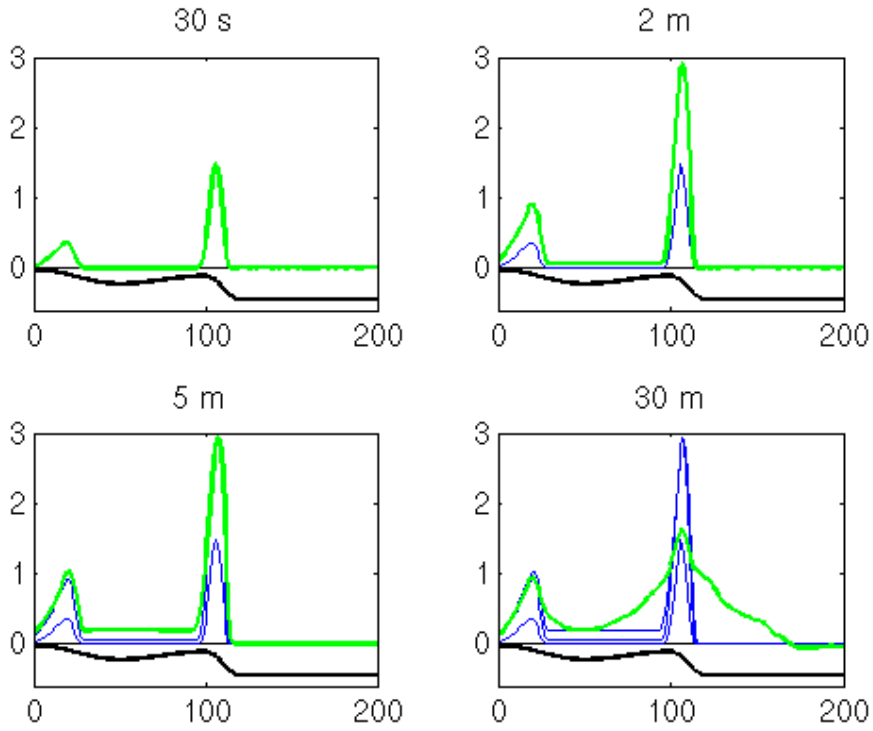

Figure 5.7: Early development of mean longshore current for simulation B

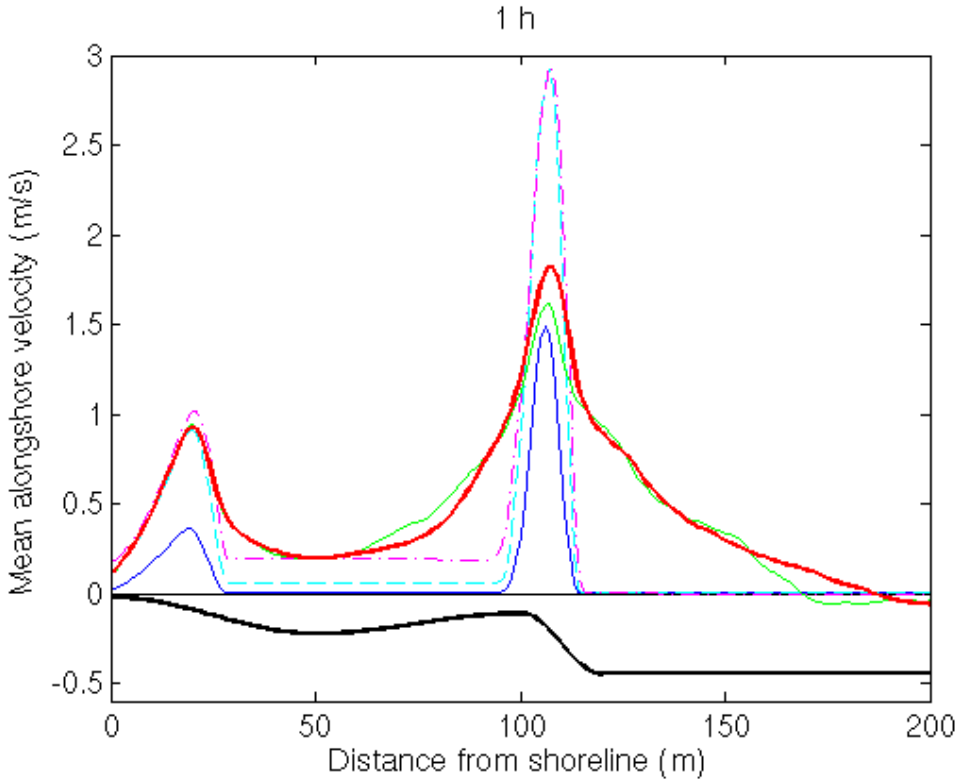

Figure 5.8: Early development of mean longshore current for simulation B

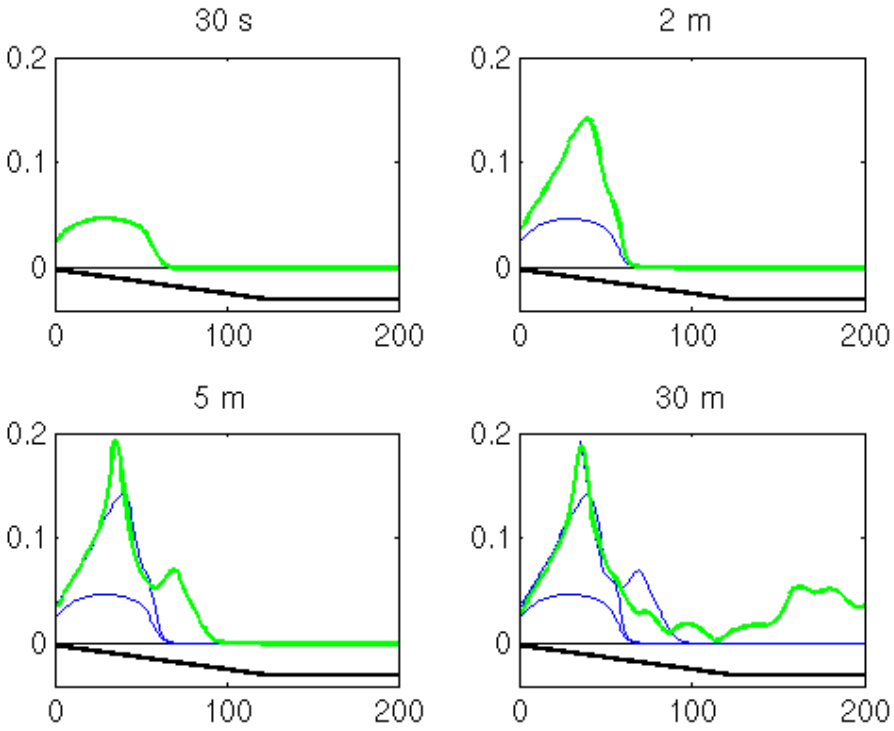

Figure 5.9: Early development of mean longshore current for simulation C

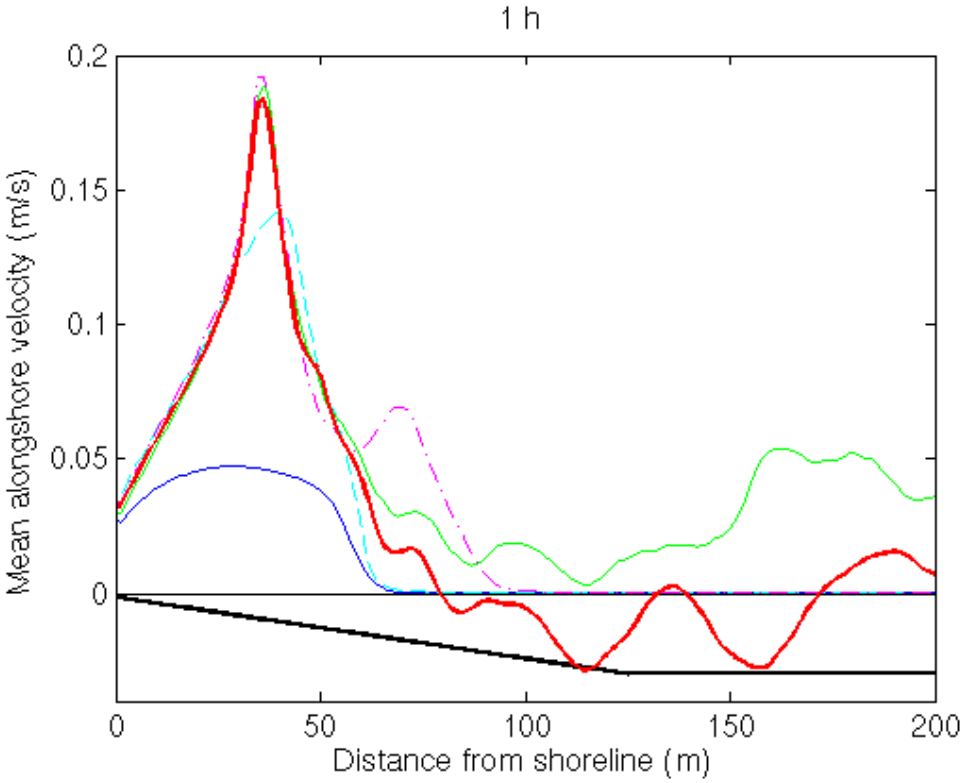

Figure 5.10: Early development of mean longshore current for simulation C

5.1 Long-time observations

In the previous section, we examined the evolution of the nearshore current structure from rest over the period of about 30 minutes. However, experimental data is typically averaged from instantaneous measurements over a period of time comparable to this length of time (in DELILAH, current measurements were processed in 34 minute increments) and the current structure is relatively steady over a period of hours. So it is important to demonstrate that the mechanism for current dislocation that we have proposed can persist over a number of hours of simulation time, or even be a steady state.

We demonstrate this by plotting the alongshore-averaged alongshore velocity for a long-running version of simulation A (up to 14 hours). We see a persistent spike in velocity at the trough (50 meters).

Over time, a marked current develops outside of the surf zone. This is a consequence of the peculiar vortex dynamics of the isolated packet; as the vortex dipole advects out of the trough and separates, it spins off small coherent vortices that travel down the beach until they meet their "mate" near the periodic boundary. These vortices now travel shorewards and transport some momentum offshore. Exacerbating this trend is a second circulation dipole generated at the shoreline; this circulation also gets swept offshore. This second dipole structure is an artifact of the isolated packet and we do not expect to see it in more general idealized or realistic models of wave dissipation forcing.

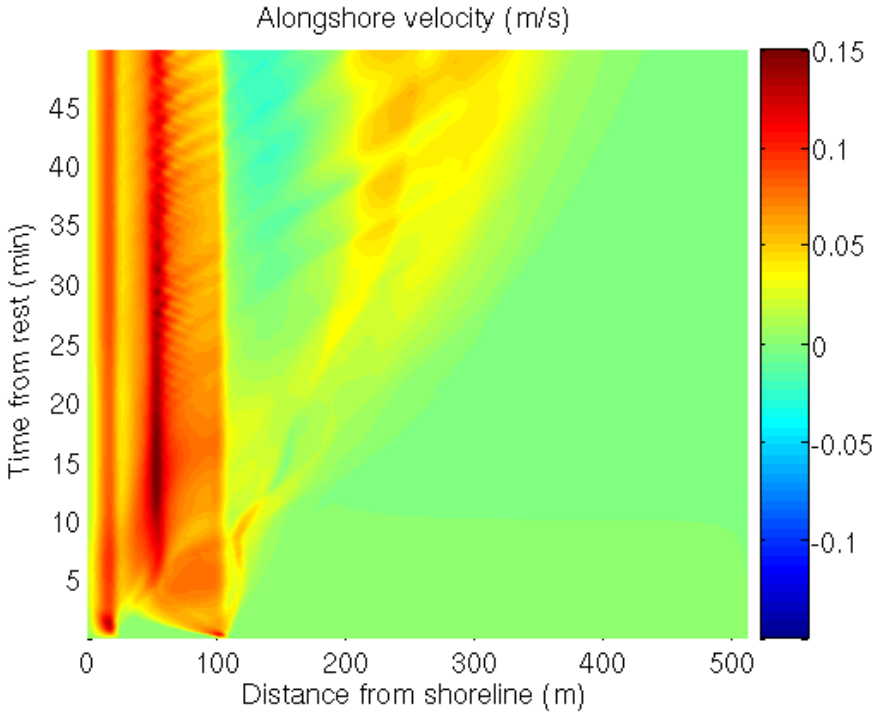

Figure 5.11: Alongshore-averaged alongshore velocity for simulation A.

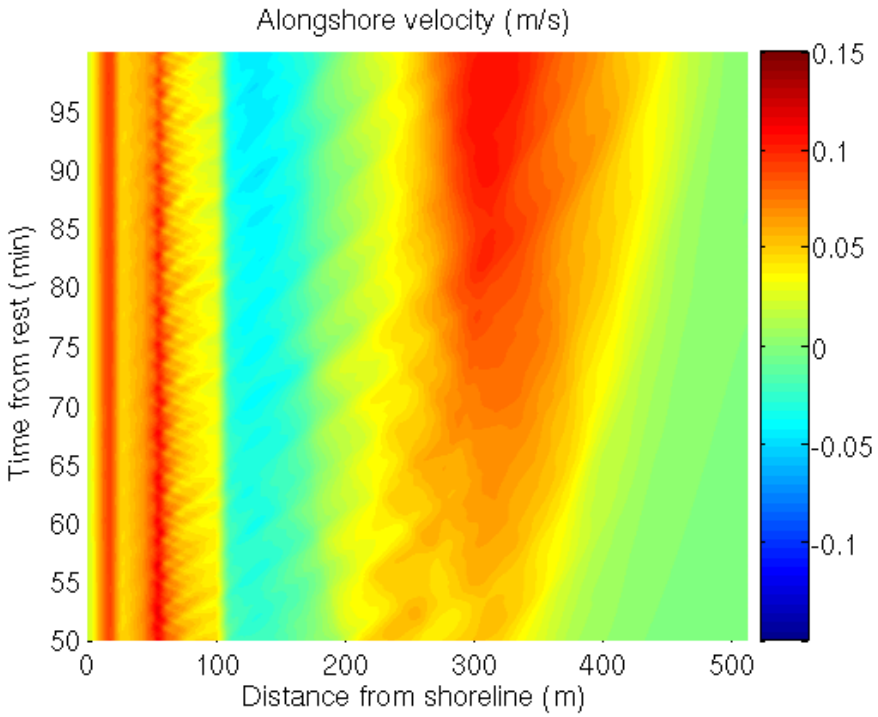

Figure 5.12: Alongshore-averaged alongshore velocity for simulation A. Continuation of previous figure

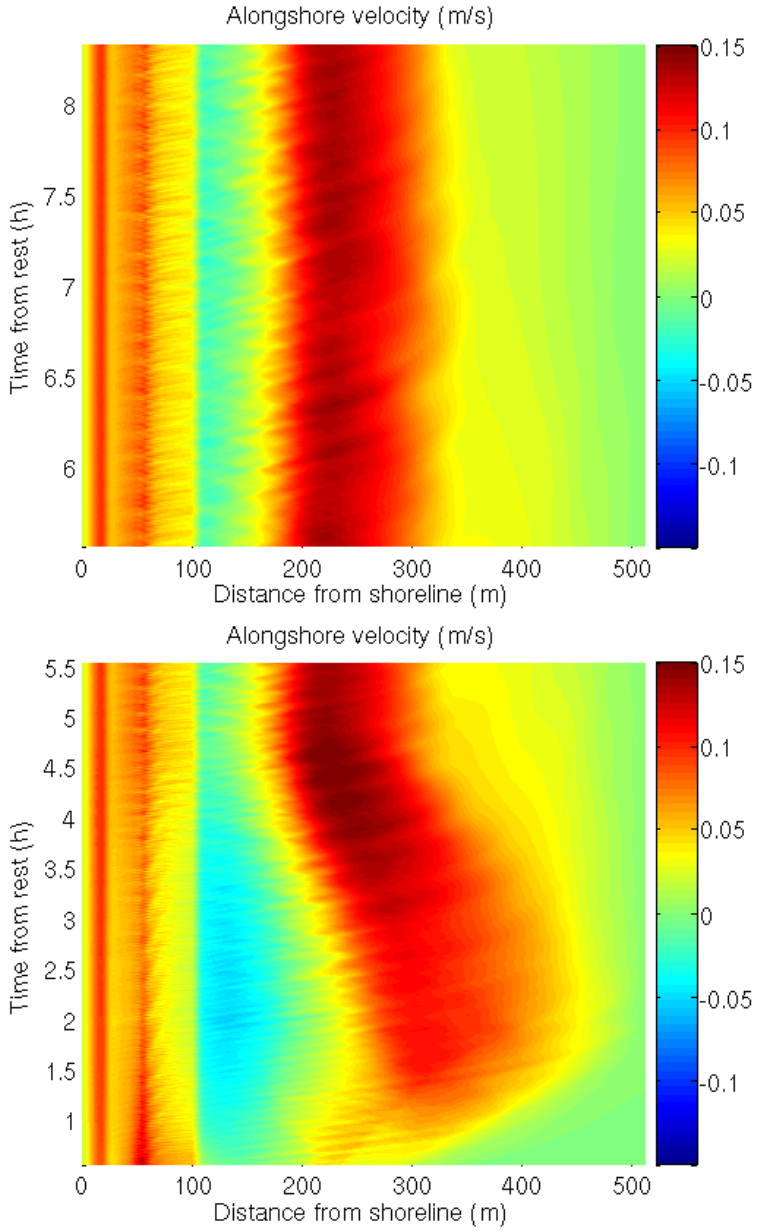

Figure 5.13: Alongshore-averaged alongshore velocity for a long-running version of simulation A. In total, this simulation was run for 14 simulation hours. **Note: the time scales on these plots are not the same**

5.2 Comparison with NLSW simulations

These results were previously achieved using a shock-resolving non-linear shallow water (NLSW) model and discussed in [10]. It is instructive to compare the computational time required in each case. The NLSW model, because it resolves surface gravity waves, has a time step that is limited to the maximum gravity wave speed present in the model. We have a computational savings because our time step is limited only by the slow vortical flow. A typical maximum velocity speed in a fully developed flow is around 2 m/s, whereas the maximum gravity wave speed in the NLSW simulations was 6.3 m/s. So from this consideration alone, we can expect a factor of three increase in time step.

In addition, the non-linear behavior of waves in the NLSW model is very different from what we wish to model in an ocean setting. For example, waves in the NLSW model will steepen and break as they travel over flat topography, whereas a linear surface ocean wave will travel unchanged. For the numerical examples presented in [10], the initial wave amplitude had to be chosen to be very small, in order that the waves would actually break over the bar and not in the off-shore region. While the vorticity forcing is qualitatively similar in shape and sign to that produced by parameterization, its magnitude differs by the relative input of energy between the two simulations.

By observing that the shallow water equations

$$\begin{aligned} \frac{\partial h}{\partial t} + \nabla \cdot (h\boldsymbol{u}) &= 0 \\ \frac{D\boldsymbol{u}}{Dt} + g\nabla(h + h_B) &= \boldsymbol{F} - \frac{c_f}{h}|\boldsymbol{u}|\boldsymbol{u} \end{aligned}$$

are invariant under the transformation

$$\begin{aligned} \boldsymbol{F} &\rightarrow \beta\boldsymbol{F} \\ \boldsymbol{u} &\rightarrow \beta\boldsymbol{u} \\ t &\rightarrow \frac{1}{\beta}t \end{aligned}$$

we conclude that the effect of magnifying a forcing by β will be to accelerate the flow by β; that is, a time period of T in the new model is equivalent to a time period of βT in the NLSW model.

It remains to establish the ratio by which the magnitude of the forcing has been increased (roughly). Let us compare the path ($\boldsymbol{x}$,$\boldsymbol{k}$,a) of a surface gravity wave in the NLSW model with that ($\tilde{\boldsymbol{x}}$,$\tilde{\boldsymbol{k}}$,$\tilde{a}$) of a gravity wave in our model. Because the path in physical and wave number space depends only on the linear dispersion wave relationship, we have $\tilde{\boldsymbol{x}} = \boldsymbol{x}$,$\tilde{\boldsymbol{k}} = \boldsymbol{k}$. Suppose that the amplitude path is given by a linear proportionality; that is $\tilde{a} = \gamma a$. Then

$$\tilde{\mathscr{F}} = \gamma^2 \mathscr{F}$$

So we should take $\beta = \gamma^2$.

In practice, we do not believe that it is useful to estimate β and draw strong conclusions from its numerical value. While the momentum input from wave dissipation should increase quadratically with the amplitude of incoming waves, the imprint of the forcing function changes shape as the amplitude increases because it depends on the onset of breaking, a highly nonlinear process. So a straight-forward "speeding up" of the flow development is not guarenteed. However it is clear that the steady flow of interest develops much faster in the vortical model (compare figure 5 and [10], figure 9); and this is certainly possible because of the use of qualitatively similar, but much stronger forcing.

Finally, the non-linear shallow water scheme used previously is extremely diffusive, particularly of enstrophy.

Chapter 6

Waves that will cause dislocation can be characterized by their breaking fraction

The previous experiment demonstrates that the vorticity dynamics proposed are active when a steady, isolated wave packet breaks on the beach. A key feature of that experiment is that the surf zone was forced by a dipole-like vorticity structure; instabilities that arise in flow with homogeneous forcing are not sufficient to create dislocation.

However, not all periodic vorticity profiles will create the same current structure. A barred beach will exhibit seaward flowing rip currents at locations where it has "cuts", because the vorticity dipole is oppositely aligned[24, 9]. To clarify the nature of the vortex dynamics produced by inhomogeneous wave

groups we construct an experiment motivated by the simulations of Reniers et al. [44, 42]. Reniers et al. examine the behavior of bathymetry under random wave forcing. Using a Jonswap frequency spectrum[1] and random phases, boundary conditions for the incoming waves in terms of time and alongshore position are computed. The amplitude of the incoming waves from a single realization show remarkable variations on the order of $O(100\ s)$ and $O(100\ m)$. The authors, however, used waves with a mean 0° direction, and so consistent longshore currents would not have been present in their setup.

We wish to examine the effect of comparable variations on the development of alongshore currents. We use the barred beach domain as described in Chapter 5. The angle of attack of the waves is fixed at 15°. The incoming wave amplitude at the seaward boundary is sinusoidal, with two periods in the domain. The amplitude and the offset may vary over the series of experiments. The effect of this variation is to change the average amplitude of the wave field; most importantly, to alter the intensity and spatial variation of wave breaking at the bar.

As the average seaward amplitude of the waves increases, the spatial fraction of the incoming wave the exceeds the saturation criterion at the bar increases; more of the wave "topples over" and breaks. Recall that a wave packet produces vortices at its flanks; what we have then is a sequence of vortex pairs, where from experiment to experiment we vary the ratio of the distance

[1]The Jonswap frequency spectrum is a wave spectrum projected to be forced by winds of a given velocity U acting over an area F or "fetch"[51]

between positive/negative pairs (shoreward-travelling) and negative/positive pairs (seaward-travelling). It is reasonable to suppose that this ratio will control whether the vortices form seaward-travelling pairs (and therefore current dislocation) or shoreward-travelling pairs (rip currents). Therefore we characterize each experiment by its "breaking fraction" (f_b), defined as the spatial percentage of the wave that breaks at the bar. For $f_b = 0.5$, each consecutive vortex should be evenly spaced from its leftward and rightward neighbor. For $f_b \ll 0.5$ we get the isolated packet regime, for $b_f \gg 0.5$ the rip current regime.

To be specific, we allowed the offset of the incoming amplitude to vary by 0.02 from 0.02 to 0.16 and the amplitude to vary by 0.04 from 0.2 to 0.2 (all numbers are fractions of the still water height 4 m at the seaward boundary). Values were discarded if a) the resulting wave-train has very weak or no breaking over the sandbar, or b) strong breaking occurred everywhere along the bar[2]. In summary the dimensional amplitude at the seaward boundary was defined to be

$$(4\ m)\left(O + A\sin(\frac{4\pi}{L})\right)$$

For each of these simulations, we ran until a stable, quasi-periodic flow emerges, as in the "packet" experiment. Then we averaged the alongshore velocity in the alongshore direction and in time (over the second half of the experiment, for $t > 1\ h$). In each case, there is a maximum alongshore velocity developed near the shoreline, where the majority of wave dissipation occurs. However, there is a second maximum between 35 m and 110 m from the

[2]These were qualitative judgments.

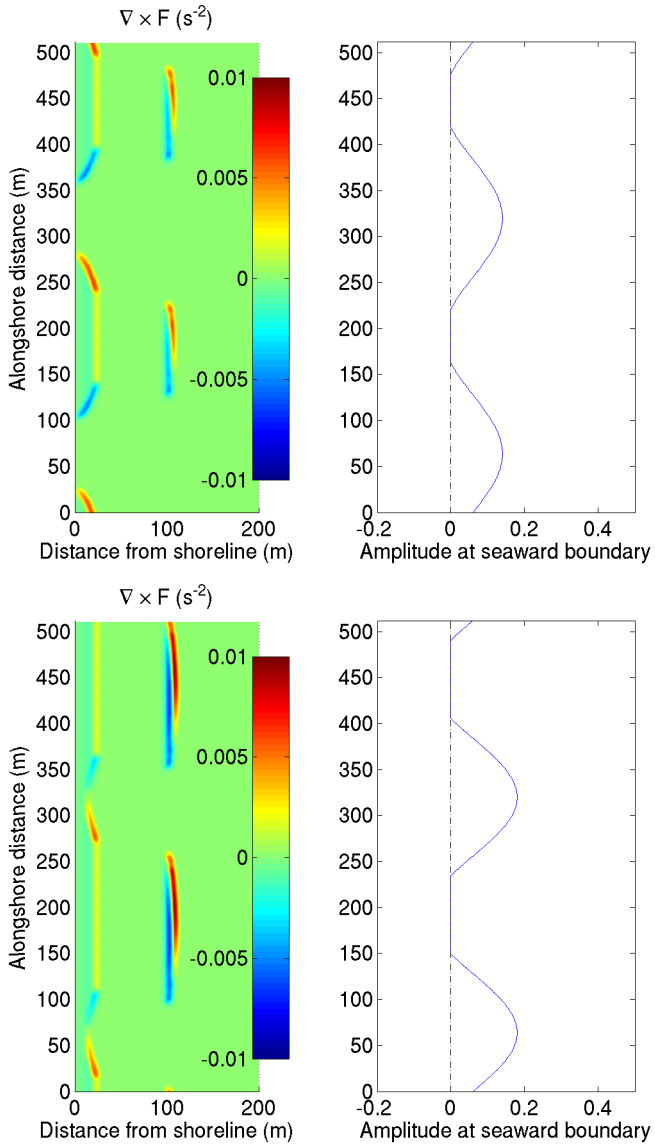

Figure 6.1: Amplitude at seaward boundary and vorticity forcing footprint for $O = 0.06$, $A = 0.08$ (top) and $O = 0.12$, $A = 0.08$. O and A are in each case expressed as a fraction of the still water depth at the seaward boundary. The location of high amplitude forcings in the side-by-side plots do not appear to "match up" because of the oblique direction of the waves.

Parameter	Definition	Formula or value
CFL	Courant-Friedrichs-Levy number	< 0.9
Δt	Time step	$\frac{CFL}{\max \lvert \mathbf{u} \rvert} \frac{1}{1/\Delta x + 1/\Delta y} s$
Δx	x (cross-shore)-grid spacing	$2\,m$
Δy	y (alongshore)-grid spacing	$2\,m$
D	Cross-shore dimension	$512\,m$
L	Alongshore dimension	$512\,m$
h_{S_0}	Still-water depth at seaward boundary	$4\,m$
θ	Angle of incidence at seaward boundary	15
κ	Magnitude of wave-number vector	$0.29\,m^{-1}$
λ	Wave-length	$2\pi/\kappa$

Table 6.1: Parameters common over all simulations

$O \setminus A$	0.04	0.08	0.12	0.16	0.2
0.02	X	0.19	0.31	0.36	0.39
0.04	X	0.30	0.37	0.41	0.43
0.06	0.27	0.39	0.43	X	X
0.08	0.45	0.47	0.48	X	X
0.1	0.61	0.55	0.54	X	X
0.12	0.82	0.64	0.59	X	X
0.16	1.0	0.87	0.71	X	X

Table 6.2: Breaking fraction matrix: shows simulations that were retained. An "X" denotes that the simulation was discarded.

shoreline (the trough has its deepest point at 50 m, and the bar its highest point at 100 m). The location of this maximum corresponds extremely well to f_b; for $f_b < 0.6$ the second maximum is located at or near the trough low; for $f_b > 0.6$ the second maximum is located at or near the bar crest.

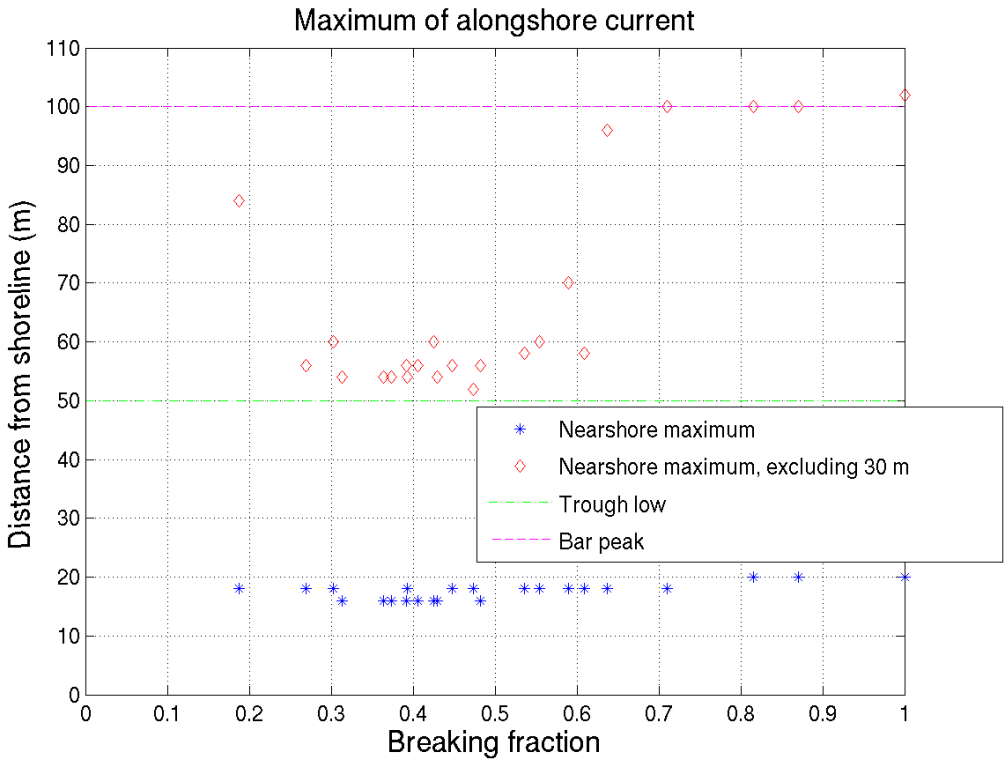

Figure 6.2: Location of current maximum vs. breaking fraction f_b for frequency-2 sinusoidal wave forcings

6.1 Discussion

While this is a promising result, a couple caveats should be mentioned. While quadratic (approximated as littoral plus quadratic mean flow, as described in §2.3.3) friction is used, there is no additional dissipation that acts preferentially at small scales (quadratic and linear drag act preferentially at large spatial scales[50, 17]). As can be seen in figures 6.3 and 6.4, significant small-scale noise is present and increases as time goes on. This noise is clearly numerical,

an artifact of the advection scheme used. However, it is unclear how use of a different scheme might alter the results.

Also, the maxima plotted in figure 6.2 are not nearly as prominent as experimental maxima, at least in comparison to the nearshore maximum, which is present in every experiment. The prominence of the nearshore maximum is related to the strong disspation due to wave breaking near that location. This would be affected by the construction of the incoming wave train, as well as by the wave-breaking model. For example, the "random wave model" described in §4.2.1 will, for typical parameters, increase the energy dissipated over the bar relative to the shoreline (relative to the saturation model used here), possibly ameliorating this behavior.

Finally, the wave breaking model may affect another aspect of the result, the location of the current maximum for a particular incoming wave-train. In particular, the circulation footprint produced by the random wave model may be shifted further shoreward (see figure 4.5), increasing the likelihood that it will travel shorewards.

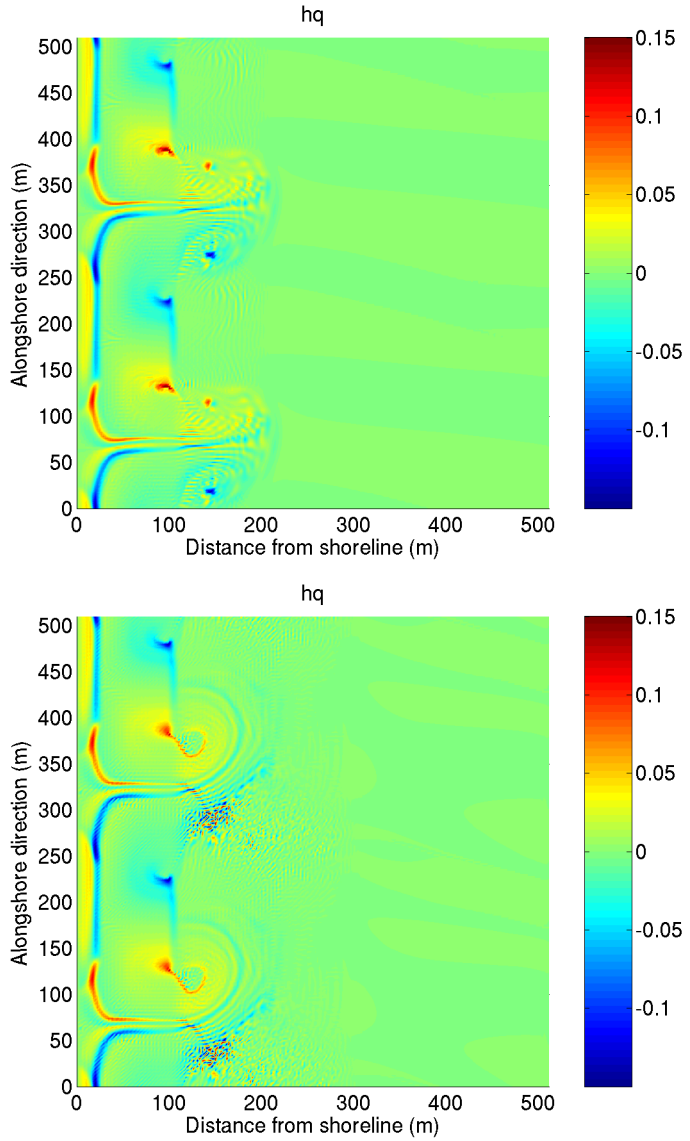

Figure 6.3: Two circulation plots from $O = 0.06$, $A = 0.08$ ($f_b = 0.39$); 30 minutes after spin-up from rest (top), 2 hours from rest (bottom)

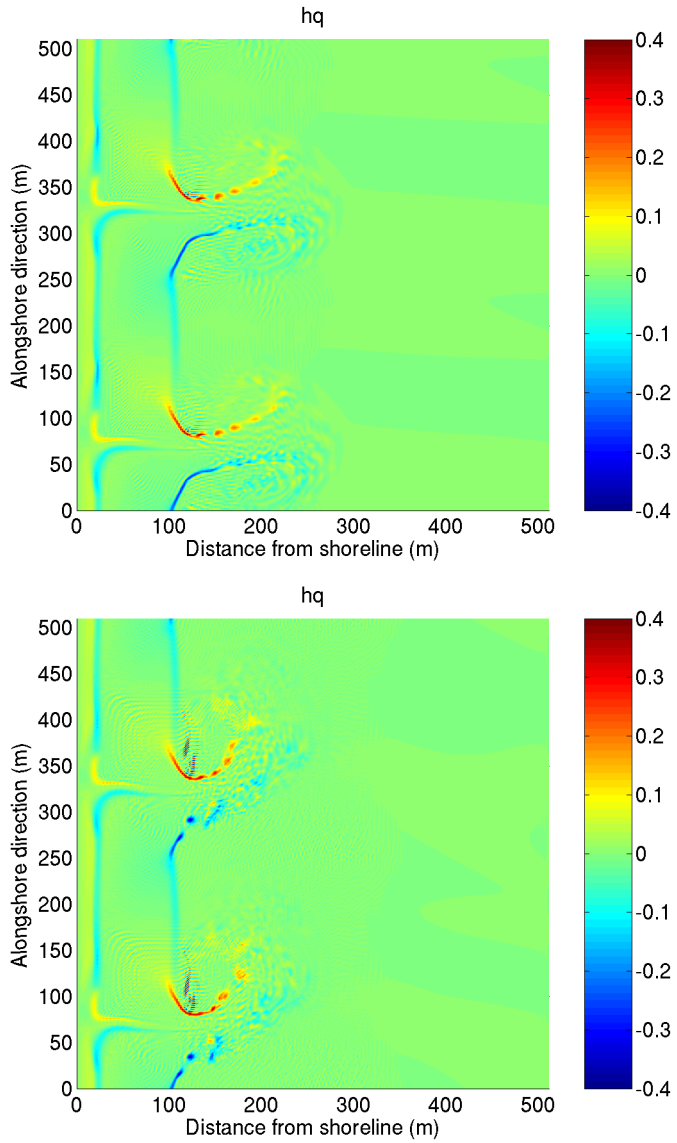

Figure 6.4: Two circulation plots from $O = 0.12$, $A = 0.08$ ($f_b = 0.39$); 30 minutes after spin-up from rest (top), 2 hours from rest (bottom)

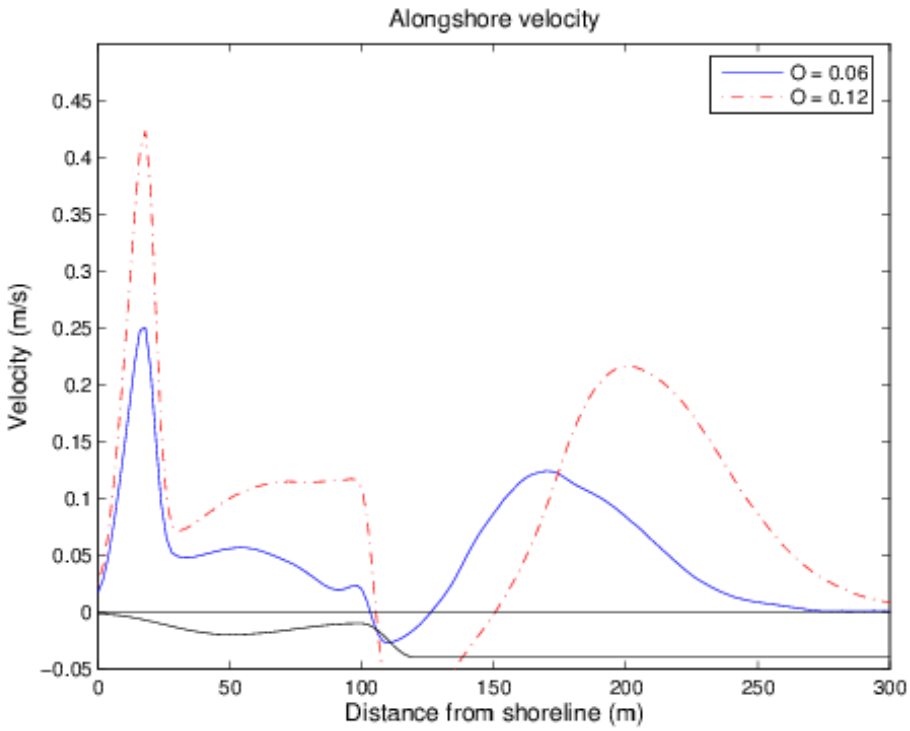

Figure 6.5: Time-averaged, alongshore-averaged alongshore currents from two experiments, $O = 0.06$ and $O = 0.12$, both with $A = 0.08$.

Chapter 7

Shallow-water turbulence with topography

Turbulent fluids are characterized by motions on a wide range of spatial and temporal scales. This requires a statistical description of the behavior; without such a description, transport and energy dissipation within the fluid cannot be understood; for example, the mean velocity at a point, unlike the mean velocity in a laminar fluid, is a completely uninteresting quantity (in an isotropically forced and dissipated fluid, the mean velocity at any point $\boldsymbol{x}$ must be zero, no matter how vigorous its motions may be[1]).

We wish to ask to what degree the near-shore current system is turbulent. Specifically, we want to know to what degree the flow shows the characteristics

[1]If the statistics of the fluid don't depend on spatial variation, a mean velocity at one point would imply the same mean velocity at any other point. But this would imply that momentum in this direction was imparted to the flow by the forcing or dissipative operators, which are statistically independent of direction.

of two-dimensional turbulence. We will find, based on recent theory for the arrest scale of quadratically dissipated systems[17], that our model in fact can not display a range of scales in which upscale energy transport can occur. This is consist with our observation that simulations of wave-forced dynamics on the beach do not show vortex mergers or energetic vortex-vortex interactions.

7.1 The near-shore current system is non-turbulent

One question we wish to address is the degree to which two-dimensional turbulence is operating in the near-shore current system. Without friction and forcing, and assuming a flat topography, the shallow water equations with a rigid lid are identical to the two-dimensional incompressible Euler equations

$$\begin{aligned} \frac{\partial q}{\partial t} + J(\psi, q) &= 0 \\ \nabla^2 \psi &= q \end{aligned}$$

The turbulent behavior of solutions to these equations has been extensively analyzed in the fluid dynamics and physics literature[57, 26], and has many interesting characteristics. If one attempts to construct a power-law relationship for the kinetic energy at equilibrium (assuming that there is both a source and a sink of energy), one finds that a two-dimensional fluid, if it is forced at some intermediate spatial scale relative to the domain size, must have an upscale

cascade of energy and a downscale cascade of enstrophy.

The mechanism by which these energy and enstrophy scales tranfers are accomplished is through vortex straining and mergers (cite Ecke here). Straining and creation of filaments allows enstrophy to go to smaller scales, while merger of vortices sends energy to larger scales. If unchecked by some energy dissipation mechanism at large scales, the size of features may expand to the domain size. Mechanisms that dissipate energy at large scales include linear or quadratic friction; in particular the friction that we employ in our model of the near-shore region.

Grainik et al. [17] analyze the cascade phenomenology of shallow water of uniform depth h

$$\frac{\partial \xi}{\partial t} + \boldsymbol{u} \cdot \nabla \xi = F_\xi + D_\xi \tag{7.1}$$

$$D_\xi = \nabla \times (-C_d |\boldsymbol{u}| \boldsymbol{u}) \tag{7.2}$$

C_d is the combination of a non-dimensional friction parameter and the layer depth; that is $C_d = c_f/h$, in our earlier terminology. F_ξ is assumed to be isotropic and isolated in wavenumber space, near wavenumber k_f. As in the traditional two-dimensional picture, in equilibrium energy will cascade to larger scales. At some scale k_a, however, friction will overwhelm the non-linear energy transfer of energy and "arrest" the cascade. Grainik et al. identify k_a

by matching the advective time scale to the drag time scale

$$\begin{aligned} T_{adv} &\sim k^{-2/3}\epsilon^{1/3} \\ T_{drag} &\sim C_d^{-1}k^{1/3}\epsilon^{1/3} \end{aligned}$$

and find that they are matched at the wavenumber

$$k_a = A_n C_d \tag{7.3}$$

that is, k_a depends only on C_d. Therefore knowing the friction coefficient and the layer depth, we should be able to predict the arrest scale.

Grainik et al. find experimentally that the arrest scale is indeed unchanged by varying the energy input, and that

$$k_a \approx 51 C_d$$

A_n is also estimated by assuming that the quadratic drag is well approximated by a linear drag

$$\begin{aligned} D_\xi &= -C_d|\boldsymbol{u}|\xi \\ &= -r_{eff}\xi \end{aligned}$$

for $r_{eff} = C_d|\boldsymbol{u}|$. When $|v|$ is chosen to be the velocity at the arrest scale, and the scale itself is chosen as the arrest scale of the corresponding linear drag

[50], yielding possible values of $A_n = 32.4$ and $A_n = 54$, using two different estimates of the corresponding linear constant.

k_a is naturally related to the vertical aspect ratio of the shallow layer; the horizontal scale at which turbulence is arrested is much larger for a shallow layer than for a deep layer. In particular, suppose that we are considering motions for which the shallow water equations are considered to be a good model for a shallow, three-dimensional layer of fluid; this requires that

$$kh < 1$$

where k is a characteristic scale of the motions.

This is the assumption that we must make in order to model the beach [2]. But the arrest scale on the beach must occur at

$$\begin{aligned} k_a &= 51\frac{0.01}{h} \\ k_a h &= 0.5 \end{aligned}$$

Regardless of the local depth of the fluid, any turbulence is arrested at only twice the scale of the smallest resolvable motions. There is no possibility then, of cascade to larger scales.

This conclusion should be taken with caution. First, the results of Grainik et al. assumed constant h and isotropic forcing. It is not clear how to general-

[2] in fact, the discretization choices that we make in our model typically do not resolve scales below this; that is the ratio of horizontal grid spacing to fluid depth is approximately 1

ize to variable h and the spatially-localized, deterministic forcing used in the beach simulation. We have asserted that any forcing on a scale appropriate to shallow-water modelling would be arrested by the quadratic drag. This could be clarified by examining simulations where the scale of forcing is varied.

Another point of concern is the use of shallow water with quadratic drag to model the near-shore region. This is a common modelling assumption and is based on the idea that the shear stress on the current due to bed friction is due to a turbulent boundary layer. In a shallow water model, this stress is considered to be distributed equally throughout the layer and the constant c_f is typically assigned a constant value, resulting in the momentum conservation equation term $c_f \frac{\mathbf{u}|\mathbf{u}|}{h}$. Spatial variation in the coefficient is sometimes used (as in reference [15]), and experimental studies suggest that breaking waves have a larger influence on the behavior of the boundary layer than just by varying the free-stream velocity of the breaking wave[38]. Finally the numerical determination of a constant (or a spatial varying c_f) has resulted in variations over different beaches and different conditions, without a clear rationale for how to generalize to unmeasured beaches. In conclusion, quadratic drag is known to be a rough and inaccurate representation of the shear stress from the bed.

Finally, we should address the ability of our numerical model to simulate forced-dissipative turbulence. Currently, we employ no small scale enstrophy filter, which is necessary for any forced simulation of isotropic turbulence. In order to properly reproduce the simulations given in Grainik et al. (or an analogue for the sloping beach, as suggested earlier), an appropriate dissipative

operator will need to be used.

Bibliography

[1] L.V. Ahlfors. *Complex Analysis*. McGraw-Hill, Inc., 3rd edition, 1979.

[2] J.S. Allen, P.A. Newberger, and R.A. Holman. Nonlinear shear instabilities of alongshore currents on plane beaches. *Journal of Fluid Mechanics*, 310:181–213, 1996.

[3] D.G. Andrews and M.E. McIntyre. An exact theory of nonlinear waves on a Lagrangian-mean flow. *Journal of Fluid Mechanics*, 89(4):609–646, 1978.

[4] Randolph E. Bank and Craig C. Douglas. Sharp estimates for multigrid rates of convergence with general smoothing and acceleration. *SIAM Journal of Numerical Analysis*, 22(4):617–633, 1985.

[5] J.A. Battjes and J.P.F.M. Janssen. Energy loss and set-up due to breaking in random waves. In *Proceeding of the 16th Coastal Engineering Conference*, 1978.

[6] A.J. Bowen. Rip currents. 1. Theoretical investigations. *Journal of Geophysical Research*, 74:5467–5478, 1969.

[7] A.J. Bowen and R.A. Holman. Shear instabilities of the mean longshore current. 1. Theory. *Journal of Geophysical Research*, 94:18023–18030, 1989.

[8] A.J. Bowen and D.L. Inman. Rip currents. 2. Laboratory and field investigations. *Journal of Geophysical Research*, 74:5479–5490, 1969.

[9] M. Brocchini, A. Kennedy, L. Soldini, and A. Mancinelli. Topographically controlled, breaking-wave-induced macrovortices. Part 1. Widely separated breakwaters. *Journal of Fluid Mechanics*, 507:289–307, 2004.

[10] Oliver Bühler and Tivon E. Jacobson. Wave-driven currents and vortex dynamics on barred beaches. *Journal of Fluid Mechanics*, 499:313–339, 2001.

[11] A.J. Chorin and J.E. Marsden. *A Mathematical Introduction to Fluid Mechanics*. Springer, 3rd edition, 1993.

[12] J.C. Church and E.B. Thornton. Effects of breaking wave induced turbulence within a longshore current model. *Coastal Engineering*, 20:1–20, 1993.

[13] W.A. Berkemeier et al. The 1990 DELILAH nearshore experiment: Summary report. Technical Report CHL-97-24, U.S. Army Corps of Engineers, 1997. revised 2001.

[14] F. Feddersen and R.T. Guza. Observations of nearshore circulation: alongshore uniformity. *Journal of Geophysical Research*, 108, 2003.

[15] F. Feddersen, R.T. Guza, S. Elgar, and T. Herbers. Alongshore momentum balances in the nearshore. *Journal of Geophysical Research*, 103:15667–15676, 1998.

[16] D. Givoli, I. Patlashenko, and J.B. Keller. Discrete Dirichlet-to-Neumann maps for unbounded domains. *Computational Methods in Applied Mechanics and Engineering*, 164:173–185, 1998.

[17] N. Grianik, I.M. Held, K.S. Smith, and G.K. Vallis. The effects of quadratic drag on the inverse cascade of two-dimensional turbulence. *Physics of Fluids*, 16(1):73–78, 2004.

[18] M. Grote and J.B. Keller. On nonreflecting boundary conditions. *Journal of Computational Physics*, 122:231–243, 1995.

[19] W. Hackbusch. *Multi-Grid Methods and Applications*. Springer Series in Computational Mathematics. Springer-Verlag, 1985.

[20] W.D. Hayes. Kinematic wave theory. *Proceedings of the Royal Society of London, Series A*, 320(1541):209–226, 1970.

[21] A. Iserles. *A First Course in the Numerical Analysis of Differential Equations*. Cambridge University Press, 1996.

[22] J.W. Kamphius. Friction factor under oscillatory waves. *Journal of the Waterways, Harbors and Coastal Engineering*, 101:135–144, 1975.

[23] J.B. Keller and D. Givoli. Exact non-reflecting boundary conditions. *Journal of Computational Physics*, 82:172–192, 1989.

[24] A.B. Kennedy. A circulation description of a rip current neck. *Journal of Fluid Mechanics*, 497:225–234, 2003.

[25] P.D. Komar. *Nearshore Sediment Dynamics and Sedimentation*, chapter Nearshore currents: Generation by obliquely incident waves and longshore variations in breaker height, pages 17–45. Wiley, 1975.

[26] R.H. Kraichnan and D. Montgomery. Two-dimensional turbulence. *Reports on Progress in Physics*, 43, 1980.

[27] H. Lamb. *Hydrodynamics*. Dover Publications, Inc., 1932.

[28] M.S. Longuet-Higgins. Longshore currents generated by obliquely incident sea waves, 1. *Journal of Geophysical Research*, 75(33):6778–6789, 1970.

[29] M.S. Longuet-Higgins. Longshore currents generated by obliquely incident sea waves, 2. *Journal of Geophysical Research*, 75(33):6790–6801, 1970.

[30] M.S. Longuet-Higgins and R.W. Stewart. Changes in the form of short gravity waves on long waves and tidal currents. *Journal of Fluid Mechanics*, 8:565–583, 1960.

[31] M.S. Longuet-Higgins and R.W. Stewart. The changes in amplitude of short gravity waves on steady non-uniform currents. *Journal of Fluid Mechanics*, 10:529–549, 1961.

[32] M.S. Longuet-Higgins and R.W. Stewart. Radiation stress and mass transport in gravity waves, with application to surf-beats. *Journal of Fluid Mechanics*, 13:481–504, 1962.

[33] M.S. Longuet-Higgins and R.W. Stewart. A note on wave set-up. *Journal of Marine Research*, 21:4–10, 1963.

[34] M.S. Longuet-Higgins and R.W. Stewart. Radiation stresses in water waves; a physical discussion, with applications. *Deep-Sea Research*, 11:529–562, 1964.

[35] W.J. Merryfield, P.F. Cummins, and G. Holloway. Equilibrium statistical mechanics of barotropic flow over finite topography. *Journal of Physical Oceanography*, 31:1880–1890, 2001.

[36] D.H. Peregrine. Surf zone currents. *Theoretical and Computational Fluid Dynamics*, 10:295–309, 1998.

[37] D.H. Peregrine. Large-scale vorticity generation by breakers in shallow and deep water. *European Journal of Mechanics; B, Fluids*, 18:403–408, 1999.

[38] M. Petti and S. Longo. Turbulence experiments in the swash zone. *Coastal Engineering*, 43:1–24, 2001.

[39] U. Putrevu, J. Oltman-Shay, and I.A. Svendsen. Effect of alongshore nonuniformities on longshore current beaches. *Journal of Geophysical Research*, 100:16119–16130, 1995.

[40] B. Raubenheimer. Shaping the beach, one wave at a time. *Oceanus*, 2004. Woods Holes Oceanographic Institute.

[41] A.J.H.M. Reniers and J.A. Battjes. A laboratory study of longshore currents over barred and non-barred beaches. *Coastal Engineering*, 30:1–22, 1997.

[42] A.J.H.M. Reniers, J.A. Roelvink, and E.B. Thornton. Morphodynamic modeling of an embayed beach under wave group forcing. *Journal of Geophysical Research*, 109, 2004.

[43] A.J.H.M. Reniers, E.B. Thornton, and T.C. Lippman. Longshore currents over barred beaches. In *Coastal Dynamics '95*, pages 413–424, 1995.

[44] A.J.H.M. Reniers, A.R. von Dongeren, J.A. Battjes, and E.B. Thornton. Linear modeling of infragravity waves during delilah. *Journal of Geophysical Research*, 107, 2002.

[45] G. Richardson. Vortex motion in shallow water with varying bottom topography and zero Froude number. *Journal of Fluid Mechanics*, 411:351–374, 2000.

[46] J.A. Roelvink. Dissipation in random wave groups incident on a beach. *Coastal Engineering*, 19:127–150, 1993.

[47] R. R. Rosales. personal communication.

[48] B.G. Ruessink, J.R. Miles, F. Feddersen, R.T. Guza, and Steve Elgar. Modeling the alongshore current on barred beaches. *Journal of Geophysical Research*, 106:22451–22463, 2001.

[49] D.N. Slinn, J.S. Allen, P.A. Newberger, and R.A. Holman. Nonlinear shear instability of alongshore currents over barred beaches. *Journal of Geophysical Research*, 103, 1998.

[50] K.S. Smith, G. Boccaletti, C.C. Henning, I.N. Marinov, C.Y. Tam, I.M. Held, and G.K. Vallis. Turbulent diffusion in the geostrophic inverse cascade. *Journal of Fluid Mechanics*, 469, 2002.

[51] R.H. Stewart. *Introduction to Physical Oceanography.* self-published on the website oceanworld.tamu.edu/home/course_book.htm, 2004.

[52] I.A. Svendsen. Wave heights and set-up in a surf zone. *Coastal Engineering*, 8:303–329, 1984.

[53] I.A. Svendsen and U. Putrevu. Nearshore mixing and dispersion. *Proceedings of the Royal Society of London: Mathematical and Physical Sciences*, 455:561–576, 1994.

[54] E.B. Thornton and R.T. Guza. Transformation of wave height distribution. *Journal of Geophysical Research*, 88:5925–5938, 1983.

[55] E.B. Thornton and R.T. Guza. Surf zone currents and random waves: Field data and models. *Journal of Physical Oceanography*, 16:1165–1178, 1986.

[56] S.V. Tsynkov. Numerical solution of problems on unbounded domains. a review. *Applied Numerical Mathematics*, 27:465–532, 1998.

[57] G.K. Vallis. *Nonlinear Phenomena in Atmospheric and Oceanic Sciences*, chapter Problems and phenomenology in two-dimensional turbulence. Springer, 1992.

[58] B.S. White and B. Fornberg. On the chance of freak waves at sea. *Journal of Fluid Mechanics*, 355:113–138, 1998.

[59] H. Yserentant. Old and new convergence proofs for multigrid methods. *Acta Numerica*, pages 285–326, 1993.